N73-23073

IIT Research Institute
Engineering Mechanics Division
10 West 35th Street
Chicago, Illinois 60616

# DETERMINATION OF THE DISTRIBUTION OF SOUND SOURCE INTENSITIES IN SUBSONIC AND SUPERSONIC JETS

R. J. Damkevala
R. S. Norman

CASE FILE COPY

Final Technical Report

Contract NAS8-27011
IITRI Project J6246

February 1973

Prepared for

George C. Marshall Space Flight Center
Marshall Space Flight Center, Alabama 35812

# FOREWORD

This report was prepared by IIT Research Institute (IITRI) for the National Aeronautics and Space Administration Marshall Space Flight Center, on Contract NAS8-27011. The work described in the report was performed during the period June 1971 to February 1973.

The authors wish to acknowledge the support of several MSFC personnel during measurements at the TAJF. The use of the tape recorder and electronic instrumentation facilities was made possible by Mr. Felix and the assistance of Mr. George Kennemar was invaluable. Special mention should be made of Dr. F. Grosche and, Mr. S. Guest and Mr. G. Wilhold, S&E-AERO-AU whose technical support and guidance have proved of great value.

Mr. J. Fitzgerald and Mr. W. E. Purcell conducted much of the crossed beam setup and measurement work. Finally, the support of Col. C. L. Ferrell and Mr. M. Phillips of IITRI's Huntsville office was extremely helpful.

Prepared by

Rusi J. Damkevala
Research Engineer
Fluid Dynamics and Acoustics

R. S. Norman
Research Engineer
Fluid Dynamics and Acoustics

Approved by

Milton R. Johnson
Assistant Director of Research
Engineering Mechanics Division

RJD/mer

# CONTENTS

# LIST OF TABLES

## LIST OF FIGURES

## LIST OF FIGURES (concl)

## NOTATION

| | |
|---|---|
| $a$ | speed of sound |
| $D$ | nozzle diameter |
| $\bar{I}$ | mean signal level at detector |
| $I(t)$ | total transmitted signal |
| $I_o$ | initial radiated signal |
| $i(t)$ | fluctuating component of signal |
| $K(t)$ | absorption coefficient |
| $k(t)$ | fluctuating component of absorption coefficient |
| $L_{y_1}, L_{y_2}, L_{y_3}$ | components of turbulence scales |
| $M$ | Mach number |
| $P$ | pressure of gas mixture |
| $p$ | partial pressure of $CO_2$ in gas mixture |
| $R(\xi, \tau)$ | cross-correlation function |
| $R_L(\tau_L)$ | *moving-frame correlation function* |
| $r$ | $\underline{X} - \underline{Y}$, also radial distance |
| $S(\underline{Y}, t, \tau^*)$ | sound source integral |
| $s$ | sound source strength per unit length |
| $T$ | absolute temperature |
| $t$ | time |
| $U(r)$ | axial velocity |
| $U_c$ | convection velocity |
| $U_\rho$ | convection velocity of density fluctuations |
| $\underline{X}$ | position vector of observer outside flow |
| $\underline{Y}$, $\underline{Z}$ | position vectors of sources in flow |
| $y_1, y_2, y_3$ | coordinate axes connected to $\underline{Y}$ |
| $\xi, \eta, \zeta$ | variables along $y_1, y_2, y_3$ axis measured from $\underline{Y}$ |
| $\underline{\Delta}$ | Eulerian space variable = $\underline{Z} - \underline{Y}$ |
| $\underline{\lambda}$ | space variable in moving reference frame |
| $\rho$ | instantaneous density |
| $\rho_o$, $\bar{\rho}$ | mean density |

# DETERMINATION OF THE DISTRIBUTION OF SOUND SOURCE INTENSITIES IN SUBSONIC AND SUPERSONIC JETS

R. J. Damkevala
R. S. Norman
IIT Research Institute

## SUMMARY

Equations relating crossed beam space-time correlations to the sound source strength per unit length of an idealized jet are presented and applied to actual measurements in unheated jets at M = 0.71 and M = 1.0.

The infrared crossed beam system was assembled and checked out at the TAJF. The prediction of the system's insensitivity to temperature fluctuations when set at 4.31 microns with a 0.08 micron bandpass was checked.

Relative intensity profiles of density fluctuations for jets at M = 0.71, 1.0 and 1.94 were measured. These profiles differ considerably from velocity fluctuation profiles measured by other investigators with hot-wires. The convection speeds also differ. Finally, the sound source strengths per unit length are obtained at various axial distances for the subsonic and sonic jet. The sonic jet shows peak source strength at an axial distance of six diameters.

The description of a preliminary design for an on-line calibration chamber, which is compatible with the present crossed beam equipment, is appended to this report.

## 1. THEORETICAL BACKGROUND

### A. Introduction

If a beam of radiation passes through a turbulent fluid which modulates the beam by an absorption process, the transmitted signal I(t) can be expressed in terms of the initial unabsorbed signal $I_o$ and an absorption coefficient K(t) by Beer's Law,

$$I(t) = I_o \, e^{-\int K(t)\, d\eta} \tag{1}$$

The integration is to be performed along the radiation path from the source to the detector. The signals $I_o$ and $I(t)$ may be expressed in volts or any other convenient unit of measurement.

It can be shown (ref. 1) that the fluctuating part of the signal $i(t)$ is related to the fluctuating part $k(t)$ of the absorption coefficient and the mean signal level at the detector $\bar{I}$,

$$i(t) = \bar{I} \int k(t)\, d\eta \tag{2}$$

In the derivation of equation (2) from equation (1) the exponential is expanded into an infinite series and the higher order terms neglected. This linearization does not restrict the applicability of equation (2) to small thermodynamic fluctuations. Only the radiation wavelength should be selected such that

$$i(t) \ll \bar{I} \quad \text{or} \quad \int k(t)\, d\eta \ll 1.$$

This condition is easily satisfied by properly adjusting the length and initial strength of the radiation beam in most practical applications.

In the crossed beam arrangement, the transmission paths for two optical systems are arranged to intersect in the turbulent region of interest. If one beam is assumed to lie along the $Y_2$ direction and the other along the $Y_3$ direction, with the direction of jet flow along the $Y_1$ axis, the cross correlation function is given by

$$R(\xi, \tau) = \frac{\langle i_{y_2}(t) \cdot i_{y_2}(t + \tau) \rangle}{\bar{I}_{y_2} \, \bar{I}_{y_3}} = \int_{-L_{y/2}}^{L_{y/2}} \int_{L_{z/2}}^{L_{y/2}} \langle k(y_1, y_2+\eta, y_3, t)$$

$$k(y_1+\xi, y_2, y_3+\zeta, t+\tau) \rangle \, d\eta \, d\zeta \tag{3}$$

where

$\xi$, $\eta$, $\zeta$ variables along $y_1$, $y_2$, and $y_3$ directions

$\tau$ time delay

## B. Turbulence Intensity

When the beams intersect we have $\xi = 0$ and to a good approximation we can write

$$R(0,0) = \overline{k^2(\underline{Y})}\, L_{y_2}\, L_{y_3} \tag{4}$$

where $L_{y_2}$, $L_{y_3}$ are the turbulence radial scales. The fluctuations in extinction (absorption) coefficient can be related to the desired thermodynamic species fluctuations in the jet by selecting a suitable radiation bandpass and wavelength. The correlation function R(0,0) is thus a measure of the turbulence intensity for that particular thermodynamic species being measured, since the radial scales are relatively constant across a jet cross section (ref. 2). For the 4.31 micron beam setting, the extinction coefficient is related directly to the partial pressure or density of $CO_2$ in the fluid, and

$$R(0,\ 0)\ \alpha \langle (\rho - \rho_o)^2\ (\underline{Y}) \rangle \tag{5}$$

where $\underline{Y}$ is the position vector of the beam intersection point. We shall term $\sqrt{R(0,\ 0)}$ as the relative intensity of density fluctuations since it is proportional to $\sqrt{\langle (\rho - \rho_o)^2 \rangle}$

## C. Convection Speeds

The cross correlation function in crossed beam measurements was defined by equation (3). The transmission paths of two mutually perpendicular beams intersect at the point $Y(y_1, y_2, y_3)$ in the jet. The variables along the beams $\eta$, $\zeta$ are measured from the point of intersection. If the vertical beam is now moved downstream a distance $\xi_1$, the correlation function $R(\xi_1, \tau)$ will exhibit a maximum at a time $\tau_1$ corresponding to the convection time of the signal-producing fluctuations in the flow. For small $\xi$, this time can be used to predict the convection speed: $U_c = \xi_1/\tau_1$. This is illustrated in Figure 1 where a series of cross correlation functions are plotted for varying distances $\xi$. The envelope of the curves represents the moving axis autocorrelation function $R_L(\tau_L)$. The time delays and spacings representing the points of tangency between the moving-axis and Eulerian (fixed-beam) correlation functions can be plotted to obtain the convection speed. This form of measurement and plotting is commonly referred to as space-time correlation measurements.

If the extinction coefficient is related directly to the partial pressure or density of $CO_2$ in the fluid, these measurements will give the convection speed of density fluctuations rather than the more familiar velocity convection speed.

## D. The Sound Source Integral

Following Lighthill's approach, the far field density fluctuations are related to the effective quadruple strength $T_{ij}$ in a turbulent flow by the relation

$$\rho(\underline{X},t) - \rho_o = \frac{1}{4\pi a_o^4} \frac{(x_i-y_i)\ (x_j-y_j)}{\left|\underline{X} - \underline{Y}^{\,3}\right|} \frac{\partial^2}{\partial t^2} T_{ij}(\underline{Y},\tau_1)\,d\underline{Y} \tag{6}$$

where

$$\tau_1 = \frac{|\underline{X} - \underline{Y}|}{a_o}$$

The autocorrelation of far field density fluctuations is then given by the relation

$$\langle (\rho(\underline{X},t)-\rho_o) \cdot (\rho(\underline{X},t+\tau^*)-\rho_o) \rangle$$

$$= \frac{1}{16\pi^2\, a_o^8} \iint_\infty \frac{(x_i-y_i)\ (x_j-y_j)\ (x_k-z_k)\ (x_\ell-z_\ell)}{|\underline{X} - \underline{Y}|^3\ |\underline{X} - \underline{Z}|^3}$$

$$\frac{\partial^4}{\partial \tau^4} R_{ijk\ell}(\underline{Y},\underline{\Delta},\tau)\,d\underline{\Delta}\ d\underline{Y} \tag{7}$$

where

$$R_{ijk\ell}(\underline{Y},\underline{\Delta},\tau) = \langle T_{ij}(\underline{Y},\tau_1)\ T_{k\ell}(\underline{Y}+\underline{\Delta},\tau_1+\tau)\rangle \tag{8}$$

$\tau^*$ is an arbitrary time delay, introduced only to obtain the autocorrelation function. Equation (8) is to be evaluated at the retarded time $\tau$ given by

$$\tau = \tau^* + \frac{\underline{\Delta}\cdot(\underline{X}-\underline{Y})}{a_o\,|\underline{X}-\underline{Y}|}\ . \tag{9}$$

$\tau$ is thus a function of $\underline{\Delta}$ and is, consequently a dependent variable and should be treated as such. The coordinate system is shown in Figure 2. The position of the observer is given by the vector $\underline{X}$, while $\underline{Y}$ and $\underline{Z}$ locate the sources in the flow.

In a turbulent flow, the radiating quadrupoles are not at rest and move during the retarded time $\tau$. This motion is correctly accounted for in equation (7) since the correlation tensor $R_{ijk\ell}$, measured in the frame of the observer includes the convection effects. If we consider the time derivative of such a correlation, we find there are two contributors, the true time change and the change due to convection of space derivatives. In most turbulent flows, it is the latter which dominates, i.e., apparent changes with time are due to the instantaneous convection of space derivatives. Even though these space derivatives may be very large they do not contribute to the integral of equation (7). This can be proven by expressing volume integrals of divergence terms as area integrals which must vanish for large $\underline{\Delta}$ if

$$\lim_{\underline{\Delta}\to\infty} R_{ijk\ell}(\underline{Y},\underline{\Delta},\tau) = 0.$$

Thus, in order to present equation (7) in a form useful for noise prediction we must write it such that pure time effects are maximized. This can be done by introducing a moving frame of reference in which time scales are maximized. This of course is the frame of reference moving at the convection speed of the covariance. It must be stressed that this only <u>minimizes</u> the effects of convection of derivatives. They can be zero only in a frame which moves instantaneously with the fluid.

We define a moving axis correlation term by

$$P_{ijk\ell}(\underline{Y},\underline{\lambda},\tau) = R_{ijk\ell}(\underline{Y},\underline{\Delta},\tau) \tag{10}$$

Since an eddy at $\underline{Y}$ is convected downstream a distance $a_o\underline{M}\tau$ by the time the sound emitted at $\underline{Y}$ travels toward the observer (see Figure 2) a distance $\dfrac{\underline{\Delta}\cdot(\underline{X}-\underline{Y})}{|\underline{X}-\underline{Y}|}$, the correct variable in a frame moving at the convection Mach number is given by

$$\underline{\lambda} = \underline{\Delta} - a_o\,\underline{M}\,\tau \tag{11}$$

Combining equations (9) and (11) gives us the relationship in terms of $\underline{\lambda}$

$$\tau = \frac{\underline{\lambda}\cdot(\underline{X}-\underline{Y}) + a_o\,\tau^*\,|\underline{X}-\underline{Y}|}{a_o\left\{\underline{X}-\underline{Y} \quad -\underline{M}\cdot(\underline{X}-\underline{Y})\right\}}$$

$$= \tau(\underline{\lambda}) \tag{12}$$

It has been shown in ref. 3 that the time derivatives in the fixed and moving frames are related by

$$\frac{\partial}{\partial\tau}R_{ijk\ell}(\underline{Y},\underline{\Delta},\tau) = \left[\frac{r}{r-\underline{M}\cdot r}\frac{\partial}{\partial\tau} - a_o\,M_n\frac{\partial}{\partial\lambda_n}\right]P_{ijk\ell}(\underline{Y},\underline{\lambda},\tau) \tag{13}$$

where $\underline{r} = \underline{X}-\underline{Y}, \quad r = |\underline{X}-\underline{Y}|$

and the subscript n denotes a component normal to $\underline{M}$.

The space derivative $\dfrac{\partial}{\partial\lambda_n}P_{ijk\ell}(\lambda)$ will contribute nothing to the integral of equation (7). Differentiating three more times, equation (13) becomes

$$\frac{\partial^4}{\partial\tau^4}R_{ijk\ell}(\underline{Y},\underline{\Delta},\tau) =\!\!\!\!\!\int \frac{r^4}{(r-\underline{m}\cdot\underline{r})^4}\frac{\partial^4}{\partial\tau^4}P_{ijk\ell}(\underline{Y},\underline{\lambda},\tau) \tag{14}$$

the sign $\int\!\!\!\!=$ signifies that both sides of the equation are equivalent when integrated as in equation (7). That is, both sides of equation (14) produce the same far field effect although they are not strictly equal. Equation (7) in a moving axis frame is then given by

$$\langle (\rho(\underline{X},t)-\rho_o) \cdot (\rho(\underline{X},t+\tau^*) \rangle$$

$$= \frac{1}{16\pi^2 a_o^8} \int \frac{r_i\, r_j\, r_k\, r_\ell}{r(r-\underline{M}\cdot\underline{r})^5} \int \frac{\partial^4}{\partial\tau^4} P_{ijk\ell}\, d\underline{\lambda}\, d\underline{Y} \tag{15}$$

It is the inner integral which will concern us since it contains all the local source characteristics. We will call this integral

$$S(\underline{Y},t,\tau^*) = \int \frac{\partial^4}{\partial\tau^4} P_{ijk\ell}(\underline{Y},\underline{\lambda},\tau)\, d\underline{\lambda} \tag{16}$$

## E. Supplemental Background for Crossed Beam Subsonic Data Analysis

### 1. Jet Noise Analysis.-

Low speed case - $\underline{M} \rightarrow 0$

The quadrupole strength $T_{ij}$ in equation (6) is given by the expression

$$T_{ij} = \rho\, u_i\, u_j + (p - a_o^2\, \rho)\delta_{ij} \tag{17}$$

if we neglect viscosity.

Ribner (ref.4) considers the pressure field as composed of an ambient $p_o$, an incompressible part $p^o$ and a compressible part p with corresponding densities related by $p = a_o^2\, \rho$. It is this compressible p that contributes to the pressure fluctuations in the far field.

If a large shear gradient is present in the flow, the turbulence will tend to be most intense in that region. From the momentum equation, we get

$$\frac{\partial}{\partial t}(\rho\ u_i\ u_j) \propto P\left(\frac{\partial u_i}{\partial y_j} + \frac{\partial u_j}{\partial y_i}\right)$$

If y is in the dominant direction $\frac{\partial u_1}{\partial y_2}$ will be much larger than $\frac{\partial u_2}{\partial y_1}$, and we can write

$$\frac{\partial}{\partial t}(\rho\ u_i\ u_j) \propto p\ \frac{du_1}{dy_2} \qquad (18)$$

$$\frac{\partial^2}{\partial t^2}\left(\rho u_i u_j\right) \propto a_o^2\ \frac{\partial \rho}{\partial t}\ \frac{du_1}{dy_2} \qquad (19)$$

The crossed beam correlation function and the sound source correlation are:

$$R_E\ (\underline{Y},\ \underline{\Delta},\ \tau) = <p\ (\underline{Y},\ t)\cdot \rho\ (\underline{Y} + \underline{\Delta},\ t + \tau)>$$

$$R_{ijk\ell}\ (\underline{Y},\ \underline{\Delta},\ \tau) = <T_{ij}\ (\underline{Y},\ t)\cdot T_{k\ell}\ (\underline{Y} + \underline{\Delta},\ t + \tau)>$$

Hence:

$$\frac{\partial^4}{\partial \tau^4}\ R_{ijk\ell} \propto a_o^4 \left(\frac{du_1}{dy_2}\right)^2 \frac{\partial^2}{\partial t^2}(R_E) - a_o^4\ \frac{\partial^4}{\partial \tau^4}(R_E) \qquad (20)$$

The first term contributes to shear noise while the second term, due to homogeneous turbulence, is called the self noise term. The sound source integral

$$S\ (\underline{Y},\ t,\ \tau^*) = \int \frac{\partial^4}{\partial \tau^4}\ P_{ijk\ell}\ (\underline{Y},\ \lambda,\ \tau)\ d\lambda \qquad (16)$$

$$= \int \frac{\partial^4}{\partial \tau^4}\ R_{ijk\ell}\ (\underline{Y}, \underline{\Delta},\ \tau)\ d\underline{\Delta}$$

Hence: $$S_{shear}(\underline{Y},t,\tau^*) = a_o^4 \left(\frac{du_1}{dy_2}\right)^2 \int \frac{\partial^2}{\partial \tau^2} R_L(\underline{Y},\underline{\Delta},\tau)\,d\underline{\Delta}$$

and $$S_{self}(Y,t,\tau^*) = -a_o^4 \int \frac{\partial^4}{\partial \tau^4} R_L(\underline{Y},\underline{\Delta},\tau)\,d\underline{\Delta}$$

where the integrals have to be evaluated at $\tau^* = \tau = 0$ so that $\tau \neq (\lambda)$, and $R_L$ is measured in a moving frame of reference. Finally, the sound source strength for unit length at position $\underline{Y}$ is given by

$$s_{self} = -a_o^4 \frac{\partial^4}{\partial \tau^4} R_L(\tau) \qquad (21)$$

$$s_{shear} = a_o^4 \left(\frac{\partial U}{\partial y_2} \cos \theta\right)^2 \frac{\partial^2}{\partial \tau^2} R_L(\tau) \qquad (22)$$

This implies the directionality of the shear noise term, which is predominant at small $\theta$, i.e., close to the jet axis, becoming small in directions normal to the jet axis. Equation (22) is strictly valid only for small $\theta$ since we have assumed a dominant direction for velocity in the direction $y_1$.

## 2. Noise Spectrum.-

Referring back to equation (12), at low speeds:

$$\tau = \frac{\tau^*}{1-M \cos\theta}$$

where $\theta$ is the angle between the flow and a line joining the observer to the source. The time scale or frequency is thus multiplied by the factor $\frac{1}{1-M \cos\theta}$. This is a result of the motion of the sources relative to the observer, and tends to increase the apparent frequencies in the downstream direction.

The energy spectrum can be obtained by Fourier transformation, as

$$E_{self}\ (f_L) = a_o^4 \int \frac{\partial^4}{\partial\tau^4}\ R_L\ (\tau_L)\ \cos\ (2\pi\ f_L\ \tau_L)\ d\tau_L \qquad (23)$$

and

$$E_{shear}\ (f_L) = a_o^4 \left(\frac{du}{dy_2}\right) \cos\theta\ ^2 \int \frac{\partial^2}{\partial\tau^2} R_L(\tau_L) \cos\ 2\pi f_L \tau_L) d\tau_L \qquad (24)$$

In each of these expressions, $f_L$ is the frequency in the moving reference frame. For a fixed observer, the frequencies are doppler shifted according to

$$f = \frac{f_L}{1-M_c\ \cos\theta}$$

where $M_c$ is the convection Mach number. The total noise spectrum is given by $E_{self}\ (f) + E_{shear}\ (f)$.

Fourier transforming of the partial derivatives of moving axis crossed beam correlations $R_L\ (\tau_L)$ is best done by fitting a function of the type

$$R_L(\tau) = e^{B_1\tau + B_2\tau^2 + B_3\tau^3 + \ldots\ldots.} \qquad (25)$$

to the envelopes. The second and fourth derivatives of such an expression can be obtained analytically and Fourier transformed by means of a standard computer routine. Thus a spectrum in the moving domain will be obtained which can be transformed to the fixed frame of reference by the multiplying factor on frequency.

## 2. PRACTICAL CONSIDERATIONS

### A. Selection of Spectroscopic Settings

Based on a literature search and experimentation, the spectroscopic settings for measurements in natural air jets were narrowed down to the 4.3 micron fundamental absorption band of $CO_2$. Further experiments were conducted in a calibration cell (ref. 5) to pinpoint the relationship between the absorption coefficient K( ) and the three thermodynamic variables $\rho$, P and T.

In general, it is known that if the absorption is weak ("weak line" absorption) all rotational lines are uniformly absorbed and $K_{WL}$ is proportional to p, the partial pressure of $CO_2$ in the gas mixture. In the "strong line" region the change of gas pressure P has two effects. First, as with the weak line region, the absorber pressure p varies directly as the gas pressure P and the variations of P are directly related to the partial pressure variations. Secondly, the line width, and therefore the total effective absorption strength, varies with some power of the gas pressure P. The strong line assumption is generally valid at lower pressures where line width is sensitive to changes in pressure. The weak line assumption is generally valid where total absorption is small, regardless of pressure.

Actual measurements in a test cell at IITRI have shown that for the 4.3 micron fundamental absorption band of carbon dioxide, the weak line assumption is valid for low concentrations ($\frac{p}{P} < .1$ percent) of $CO_2$ at atmospheric pressure and above. Crossed beam measurements taken using atmospheric air will give results dominated by $CO_2$ concentration fluctuations. Since the mean $CO_2$ concentration is constant throughout the flow and its surroundings in this case, the measurements are dominated by density fluctuations. It was also found that $\frac{\partial K}{\partial T}$ was very small at wavelengths of 4.21 and 4.31 microns when a bandwidth of 0.08 micron was used. Narrower bandpasses would tend to enhance temperature effects. The present measurements were made with both beams set at 4.31 and 0.08 micron bandpass. Some measurements were also made at 4.20 and 4.35 microns at the same bandpass for future comparison purposes.

## B. Temperature Effects

The cold air jet was operated continuously and intermittantly to obtain a variation in jet stagnation temperature. During continuous operation, the stagnation temperature was maintained at 487°R. Intermittant operation allowed stagnation temperature to remain close to the ambient air temperature -- about 515°R -- although some drop occurred during the course of the run.

Figure 3 shows the results of these measurements which were made at various radial locations in the Mach 0.71 jet at an axial distance of two diameters from the nozzle. The stagnation and static temperatures in the jet are noted for each symbol used in the figure. It is observed that no correlation is evident between the measured value and the jet temperature. The scatter in measurements is larger than any temperature effects. Thus is appears that the chosen radiation wavelength and bandpass suppresses temperature fluctuations to a satisfactory degree.

The temperature variation examined in this manner is however too small to generalize the results to all conditions. Complete elimination or reversal of the static temperature gradient across the jet would require a heated jet. During present measurements the average density changes due to temperature changes were so small as to be undetectable. This will not be the case in heated jets.

### C. Effect of Beam Misalignment

During the earliest stages of crossed beam measurements, it became evident that precise alignment between the source and detector side of each beam was essential to keep the scatter of results within reasonable limits. Beam focusing, as expected, was not found to be as critical. The crossed beam instrument of MSFC was exposed to the elements during the course of measurements and even with the building doors shut the temperature in the building was not controllable. Alignment of the horizontal beam was found to be dependent on the surrounding temperature and hence frequent alignment checks were necessitated. Secondly, the detector housings appeared to jar easily, affecting the spot position on the photodetector element. If the radiation beam is not properly positioned with respect to the photodetector element, which is only 1 mm in diameter, spurious signals will be detected due to Schlieren effect.

As an illustration of the result of beam misalignment, Figure 4 shows the measured cross correlations at X/D = 4 for the Mach 1 jet. The scatter in measured values was dramatically reduced when the horizontal beam was realigned as shown by the black circles. The results shown in Figure 4 include measurements in all four quadrants of the jet cross section. Especially significant is the fact that the peak of the profile was not at all evident when the horizontal beam was misaligned. The re-alignment of the vertical beam would have required disassembly of the mirror housings. Fortunately it was found that the vertical beam held its alignment to a satisfactory degree.

## 3. TURBULENCE MEASUREMENTS

Measurements were made on an unheated air jet at MSFC. Table I lists various conditions for which turbulence intensity measurements were made. Intensity traverses are more detailed for the 315 m/sec jet and the supersonic jet with the convergent-divergent nozzle. Table II lists the space-time correlation measurements made on the same jet. At most axial locations, the space-time correlation runs were made where the turbulence intensity was maximum. The total number of runs was very large - 213 runs in the first series of August 1971 and 234 runs in the second series of December 1971. All runs were recorded on magnetic tape.

### A. Relative Intensity Profiles

The intensity traverse for the subsonic jet at 235 m/sec (M = 0.71) is shown in Figure 3 when temperature effects were discussed. The ordinate is the square root of the cross correlation measured with intersecting beams, which is directly proportional to the root mean square density turbulence intensity.

Figure 5 shows the measured intensity profiles for the Mach 1 jet at various axial distances for the nozzle. The main feature of this diagram is the location of the peak intensity at each cross section. The laminar core extends to about five diameters, with the intensity peaks closer to the jet centerline than in case of velocity fluctuations. Also, unlike velocity turbulence profiles, the turbulent density profile shows large turbulent intensities even in the core. This is presumably due to the fact that the jet core density is higher than the ambient density outside the jet and hence the fluctuations are relatively larger.

Figure 6 shows normalized relative intensity profiles plotted against the nondimensional radial distance $\eta = \frac{r/D-.5}{y_1/D}$ for the 315 m/sec jet velocity. As a comparison, the "universal" relative intensity profile for velocity fluctuations in a jet is also shown. The reason for the inward shift of the peak in case of density fluctuation profiles may be explained as follows.

If we consider density changes $(\rho-\overline{\rho})$ in the flow direction to be isotropically related to pressure changes $(p-\overline{p})$ by $(\rho-\overline{\rho}) = (p-\overline{p})/a^2$ where a is the local speed of sound, then the one-dimensional linearized momentum equation can be written as

$$a^2(r)\ [\rho(r)\ \overline{\rho}(r)]' = \overline{\rho}(r)\ U(r)\ u'(r) \tag{26}$$

where primes refer to root mean square values.

Since the local mean density will vary inversely as the local temperature T(r) across the jet, it can be shown from equation (19) that the root mean square density fluctuations are related to the local mean and fluctuating velocity by the proportionality

$$[\rho(r) - \overline{\rho}(r)]'\ \alpha\ T^{-2}(r)\ \ \frac{U(r)}{U(o)}\ \ \frac{u'(r)}{U(o)} \tag{27}$$

It is evident from this that the root mean square density profile will be weighted toward the jet centerline and the weighting will be stronger if the jet centerline temperatures are lower than ambient as is the case for unheated jets.

A set of intensity profiles for the correctly expanded supersonic jet at 485 m/sec (M = 1.94) is shown in Figure 7. The root mean square density profiles are plotted on the same scale as

Figure 5. Significantly, the "core" now extends to at least ten nozzle diameters. The intensities are higher for the sonic jet. Figure 8 is a plot of normalized root mean square density fluctuations across the supersonic jet, again plotted against the non-dimensional radial parameter $\eta$. Thus the spreading rate for the supersonic jet is far slower than the sonic jet. All profiles collapse very well, showing a peak near $\eta = -.025$, except that for $y_1/D = 2$. The reason for this is the extremely narrow extent of the mixing region at $y_1/D = 2$. Since the profiles are normalized to the measured maximum value, if the true peak of the profile lies in-between the points of measurement, the normalized profile would be in error. In this case, if the intensity at $\eta = 0$ is adjusted to be 0.7, all other points on the profile will be lowered by 30 percent and fall right on the profiles for other $y_1/D$ values. In case of $y_1/D = 12$, a secondary peak in the profile appears at $\eta = +.025$. This is most likely due to a weak shock that might be present in the jet at that location.

The intensity profiles at $y_1/D = 2$ for the underexpanded and correctly expanded supersonic jet are shown in Figure 9. This profile is plotted against the radial coordinate normalized with respect to the jet diameter. Both jets were obtained at the same stagnation pressure of 72.2 N/cm$^2$ (90 psig). The underexpanded jet used the converging 20 mm diam nozzle. Also shown for comparison is the profile for the sonic velocity jet. The underexpanded jet profile needs further study to determine the cause of the multiple peaks and the higher overall turbulence levels. It should be noted that the flow Mach number is higher than 1.94 and the pressure above atmospheric inside the intercepting shock.

## B. Space-time Correlations

A summary of space-time correlation measurements is given in Table II. It is the envelope of the space-time correlation functions that is used for the estimation of sound source properties. The space-time correlations also give the convection speed of turbulence in the flow. The measured convection speeds for each set of curves are also included in Table II. Since measurement of convection speeds was not the primary purpose of the August and December 1971 series, effort was not made to obtain complete convection speed profiles across each jet cross section.

Space-time correlations were measured on-line and also obtained from digital analysis of the recorded data. Results for the 235 m/sec jet are shown in Figures 10 through 18. In each figure the on-line measurements are shown on top. The horizontal scale (time lag) is different for digitally analyzed plots; however, comparisons can easily be made. Results for the 315 m/sec jet are shown in Figures 19 through 25. Results not included in Figures 10 through 25 are those for which digital analysis could not be performed.

Figure 26 shows the variation of convection speeds with axial distance from the nozzle. In case of hot-wire measurements, the convection speed ratio $U_c/U(o) \simeq 0.6$ at $r/D = 0.5$ and $U_c/U(o) \simeq 0.7$ at $r/D = 0$ for small axial distances. In contrast, the density turbulence convection speeds $U_\rho$ are in general higher, about 0.7 U(o) at $r/D = 0.54$. In case of the subsonic jet, at small $y_1/D$, $U_\rho/U(o)$ is between 0.6 and 0.5. It shows a sudden jump to 0.77 at $y_1/D = 3.5$ and again drops slowly with axial distance. A similar but smaller jump appears in case of the sonic jet at $y_1/D = 6.0$. These axial distances are near the ends of the laminar cores for the respective jets and indicate a weighting toward local jet velocities U(r).

## C. Jet Noise

1. Results.- Only relative results could be obtained from the present generation of crossed beam instrument. The results are in electrical units, i.e., in terms of the output of the photodetector. The conversion factor is more fully discussed in the appendix where the preliminary requirements for a calibration cell are described. Care in alignment is of primary importance and a larger number of data points would have been valuable. The extra care needed in alignment slowed down the data acquisition. The scatter in absolute values of results is such that considerable time had to be spent in the subsequent analysis phase. As a result of the

experiences on the test program, several modifications were made to the crossed beam system to give greater precision and speed in aligning the equipment. These modifications included the installation of mechanical counters on the positioning screws to provide absolute references, a general tightening up of backlash and clearances, and the reconstruction of the photodetector housings.

2. Sound Source Distribution.- For the unheated subsonic jet at M=0.71, the low speed formulations derived in Section 1-E are applicable since the actual convection Mach numbers will be of the order of 0.5, and compressibility effects small.

Envelopes of the space-time correlation functions were drawn and the exponential function $R_L = e^{B_1|\tau| + B_2|\tau|^2 + B_3|\tau|^3}$ was fitted to each envelope by means of a nonlinear least squares computer routine. One might recall that the correlations are expected to be symmetrical about the $\tau = 0$ axis. This is achieved by taking the modulus of the time lag $\tau$ rather than by omitting odd powers of the exponent. This resulted in a better fit of the function using fewer terms in the exponent. However, a discontinuity will be present at $\tau=0$ which is probably not present in the actual data, and the values of the derivatives at that point are somewhat in question. Another new feature of this routine was to fit the slopes of the functions by the method of least squares rather than fit the function itself. This resulted in more consistent higher order derivative data.

The predicted derivatives reflect the quality of the measured data. In those cases where measurements were detailed, i.e., closer and more numerous beam spacings $\underline{\Delta}$ were used and consequently the function $R_L$ was well defined near $\tau = 0$, the results were consistent from run to run at a given axial location. Figure 27 shows the data (triangles) and the fitted polynomial with the second (circles) and fourth (crosses) derivatives at $\frac{y_1}{D} = 3.5$ and radial distances in the jet $\frac{r}{D} = 0.36$ and 0.54. Both these measurements are in the intense region of the shear layer and predict consistent source strengths (see Table II).

A similar set of runs at $\frac{y_1}{D} = 2$ and $\frac{r}{D} = 0.317$ gave a completely different shape of the fourth derivative profile (see Figure 28). At this axial location, the shear layer is very thin and the gradients are more intense. Hence measurements are needed at smaller radial intervals and axial beam separations. Data at larger axial locations where the jet dimensions are larger tend to be more consistent in general. Figures 29 and 30 show the fitted functions and their derivatives at $\frac{y_1}{D} = 6.0$ and 10.0. In each figure, the derivatives have the same general trends at $\frac{r}{D} = 0$. This is as one would expect in the fully developed region beyond $\frac{y_1}{D} = 5$. The second derivative is negative at $\frac{y_1}{D} = 6$ and positive (though small), at $\frac{y_1}{D} = 10$ for $\frac{r}{D} = 0.54$. This may be due to these locations having opposite $\frac{\partial^2 u_1}{\partial y_2^2}$ terms. At $\frac{y_1}{D} = 6$, $\frac{\partial^2 u_1}{\partial y_2^2}$ will be positive at $\frac{r}{D} = 0.54$ while at $\frac{y_1}{D} = 10$, it will be negative. The velocity gradients are not expected to influence the crossed beam measurements directly, but this needs to be checked.

Table III summarizes the results for the M = 0.71 case. The sound source strength per unit jet length has been computed by taking into account the electronic gains, shear layer cross-sectional areas and estimated velocity gradients. These are shown in columns 5 and 6 of the table. The shear term is zero for those radial locations where $\partial U/\partial y_2 = 0$. Finally, column 7 of the table gives the ratio of shear noise to self noise at each axial distance in the mixing region. Except for the value at $\frac{y_1}{D} = 6.0$, the ratios are consistent and agree rather well with other investigators. Chu (ref. 6) showed that this ratio was 1.7 when he used a Gaussian function to fit his data. Other investigators (refs. 7 and 8) have shown that this ratio will be close to 1.0 if the moving frame autocorrelation function is approximated by $e^{-w(\tau)}$, assuming complete separability of the four-dimensional space-time correlation function. Using a simplified model of isotropic turbulence superposed on a mean flow and a joint Gaussian probability density for $U_x(\underline{Y})$ and $U_x(\underline{Y} + \underline{\Delta})$, Ribner obtains the following relation:

$$\frac{\text{Shear noise}}{\text{Self noise}} \backsim \frac{\cos^4\theta + \cos^2\theta}{2} \qquad (28)$$

i.e.,

$$\frac{\text{Shear noise}}{\text{Self noise}} \leq 1$$

This condition is closely approximated in our case at $\frac{y_1}{D} = 10$ and our value of 0.667 for $\theta = 0$ appears to be good.

For the M = 1.0 case, both self and shear noise terms peak at $\frac{y_1}{D} = 6$. The source strength variation appears to be relatively "smooth" for this jet and is shown in Figure 31.

3. Far Field Noise Spectrum.- The Fourier transform of the derivative functions will give the spectra. The discontinuity at $\tau = 0$ will not in general be crucial to the results except for very high frequencies. Correction should be applied to the frequencies to account for the doppler shift at small $\theta$. Using an average convection Mach number $M_c = 0.5$, the frequencies will not be shifted at $\theta = \frac{\pi}{2}$, and they will be doubled at $\theta = 0$. Ribner's analysis (ref. 7) and Chu's measurements using a hot wire anemometer (ref.6) indicate that the self noise will have a dominant frequency about 2 to 2.5 times that of shear noise. Our results, using completely different techniques, tend to confirm this. Figure 32 shows the spectra at $y_1/D = 6.0$ and $r/D = 0.54$. The overall spectrum is obtained by adding the shear and self noise spectra after the shear spectrum has been corrected for the $\left(\frac{\partial u_1}{\partial r}\right)^2$ term (equation 22). Spectra for $y_1/D=10$ are shown in Figure 33. Table IV summarizes the dominant frequencies contributed by sources at various axial and radial locations. It should be remembered that these frequencies are for the predicted far field noise, although they were obtained from measurements in the jet stream. To check our predictions with known noise spectra, we need actual measurements with this jet. Some noise measurements have been reported in

the literature and may be used as a comparison after correcting for dimensions, jet speed, etc. The noise spectrum for the whole jet can be considered as being made up of spectra from different slices of the jet. In the mixing region, the spectrum of noise from a slice of jet will have approximately the same peak as that from a unit volume at the region of maximum shear beacuse the chief noise-emitting eddies are confined in a small volume at this region. Dyer (ref. 9) has suggested that the peak frequency of the overall noise spectrum is generated by a slice located at about 5 diameters from the nozzle. The dominant frequency varies with jet velocity according to $(u_j)^{0.58}$ (ref. 10). According to Lee (ref. 11), our 25 mm (1 inch) jet at M = 0.71 (800 fps) should have a dominant frequency of 4350 Hz. Correcting our spectra from the zero degree angle, the frequencies will be increased by a factor of 2.0. We get approximately 4400 Hz at $^{y}1/D \approx 6.0$ which is very close to the prediction.

The dominant frequency varies with axial distance because the jet is growing and slowing down. At $^{y}1/D = 10$ the dominant frequency was measured as 2 x 1300 = 2600 Hz, which shows an inverse variation with axial distance.

Measurements at $^{y}1/D$ less than 6.0, for the jet mixing region failed to show a spectrum with a dominant frequency. The shear noise spectra will dominate in this region and hence more detailed measurements in the shear layer are needed before any conclusions can be drawn.

One field measurement with a microphone at 30 deg from the jet axis showed that the spectrum of the overall jet noise peaked in the 3.15 kHz 1/3 octave band, which would place the chief noise producing region of this jet somewhere between 6.0 and 10.0 diameters from the muzzle.

## 4. CONCLUSIONS AND RECOMMENDATIONS

A start has been made toward the use of the crossed beam correlation technique for studying jet noise characteristics. In many respects, the technique produced results that agree well with the results of other researchers.

The experiment pointed out the importance of detailed prior information of the structure of turbulence before meaningful source estimates can be made. It appears that the density (or pressure) fluctuations within the jet have quite a different structure from the usual velocity turbulence as measured by a hot-wire anenometer.

For future work, it would be advantageous to first make detailed measurements on a larger, 4 inch diameter jet, with and without heating. Measurements in the mixing region will have to be especially detailed. The present measurements on the 1 inch jet are deficient in this area.

A calibration cell should be built at the earliest opportunity and a technique for its routine use established. Absolute thermodynamic state measurements should be possible after this, which are essential for studying extrapolation and scaling effects.

## Table I
## SUMMARY OF INTENSITY MEASUREMENTS

| Jet Velocity m/sec | Stagnation Pressure N/cm$^2$ (lb/sq in. Gage) | $y_1/D$ | r/D | Run | Nozzle | Average Stagnation Temperature °F |
|---|---|---|---|---|---|---|
| 235 | 14.3 (6.0) | 0.5 | 0 | 194 | Convergent (20 mm diam) | |
| | | 1.0 | 0.54 | 199 | | |
| | | 3.5 | 0 to 1.98 | 1, 7, 15, 23, 36, 37 | | |
| | | 4.0 | 0, .54, 1.08 | 38, 39, 54 | | |
| | | 5.0 | 0, .54 | 55, 56 | | |
| | | 6.0 | 0, .54 | 114, 72 | | |
| | | 7.0 | 0, .54 | 115, 145 | | |
| | | 8.0 | 0, .54 | 157, 148 | | |
| | | 10.0 | 0, .54, 1.08 | 160, 175, 185 | | |
| 315 | 19.2 (13.1) | 0.5 | 0, .54 | 195, 198 | | |
| | | 1.0 | 0.54 | 207 | | |
| | | 2.0 | 0 to 1.045 | 732 to 740 | | 27 |
| | | 3.0 | 0 | 208 | | |
| | | 4.0 | 0 to 1.045 | 639 to 646 | | 24 |
| | | 6.0 | 0 to 1.4 | 673 to 682 | | 42 |
| | | 7.0 | 0, .54 | 116, 117 | | |
| 315 | 19.2 (13.1) | 8.0 | 0 to 1.14 | 688 to 693 | Convergent | 36 |
| | | 10.0 | 0 to 1.14 | 699 to 705 | | 27 |
| 485 | 72.2 (90) | 2.0 | 0 to 0.762 | 552 to 559 | | 12 |
| | | 2.0 | 0 to 1.04 | 752 to 758 | Convergent Divergent | 27 |
| | | 4.0 | 0 to 1.153 | 768 to 777 | (22 mm diam) | 19 |
| | | 8.0 | 0 to 1.27 | 787 to 795 | | 17 |
| | | 12.0 | 0 to 1.385 | 806 to 814 | | 18 |

## Table II

## SUMMARY OF SPACE-TIME CORRELATION MEASUREMENTS

| Jet Velocity m/sec | Stagnation Pressure N/cm$^2$ (lb/sq in. Gage) | $y_1/D$ | $r/D$ | Run | $U_\rho/U_o$ |
|---|---|---|---|---|---|
| 235 | 14.3 (6.0) | 1.0 | 0.54 | 199-203 | 0.625 |
| | | 2.0 | 0.317 | 572-76 | .58, .745 |
| | | 2.0 | 0.445 | 535, 538-41 | 0.7 |
| | | 3.5 | 0 | 1-6 | 0.68 |
| | | 3.5 | 0.18 | 7-12 | 0.703 |
| | | 3.5 | 0.36 | 15-22 | 0.68 |
| | | 3.5 | 0.54 | 23-29 | .51, .766 |
| | | 4.0 | 0.54 | 39-43 | 0.766 |
| | | 5.0 | 0.54 | 56, 59, 60a, 63, 64 | 0.711 |
| | | 6.0 | 0 | 110-114 | 0.68 |
| | | 6.0 | 0.54 | 72, 73, 76, 77, 80 | 0.68 |
| | | 7.0 | 0.54 | 133, 136, 139, 142, 145 | 0.66 |
| | | 10.0 | 0 | 160-163 | 0.575 |
| | | 10.0 | 0.54 | 164, 169, 170, 175 | 0.595 |
| 315 | 19.3 (13.1) | 1.0 | 0.54 | 204-207 | 0.736 |
| | | 2.0 | 0 | 747-51 | 0.672 |
| | | 2.0 | 0.38 | 741-46 | 0.65 |
| | | 3.0 | 0.54 | 208-213 | 0.736 |
| | | 4.0 | 0 | 727-31 | 0.746 |
| | | 4.0 | 0.317 | 634-38 | 0.667 |
| | | 4.0 | 0.38 | 668-72 | 0.73 |
| | | 6.0 | 0 | 105-109 | 0.674 |

Table II (concl)

| Jet Velocity | Stagnation Pressure N/cm$^2$ (lb/sq in. Gage) | $y_1/D$ | r/D | Run | $U_\rho/U_o$ |
|---|---|---|---|---|---|
| 315 | 19.3 (13.1) | 6.0 | 0 | 721-726 | 0.81 |
| | | 6.0 | 0.254 | 683-87 | 0.746 |
| | | 6.0 | 0.54 | 91, 94, 97, 100, 103 | 0.667 |
| | | 7.0 | 0.54 | 117, 121, 124, 127, 130 | 0.70 |
| | | 8.0 | 0 | 716-20 | 0.825 |
| | | 8.0 | 0.122 | 694-98 | 0.761 |
| | | 10.0 | 0 | 190-93 | 0.666 |
| | | 10.0 | 0 | 706-10 | 0.725 |
| | | 10.0 | 0.255 | 711-15 | 0.570 |
| | | 10.0 | 0.54 | 176-180 | 0.666 |
| | | 10.0 | 1.08 | 186-189 | 0.570 |
| 485 | 72.2 (90) | 2.0 | 0.445 | 546-551 | |
| | | 2.0 | 0 | 759-762 | |
| | | 2.0 | 0.52 | 763-767 | |
| | | 4.0 | 0 | 782-786 | |
| | | 4.0 | 0.52 | 777-781 | |
| | | 8.0 | 0 | 796-800 | |
| | | 8.0 | 0.346 | 801-805 | |
| | | 12.0 | 0 | 815-819 | |
| | | 12.0 | 0.231 | 820-824 | |

## Table III

### SOUND SOURCE STRENGTH PER UNIT LENGTH

| $\frac{y_1}{D}$ | $\frac{r}{D}$ | Measured 2nd Derivative | Measured 4th Derivative | $S_{Shear}$ $\theta = 0$ | $S_{Self}$ | $\frac{\text{Shear Noise}}{\text{Self Noise}}$ |
|---|---|---|---|---|---|---|
| 2 | .317 | .35 $10^8$ | .046 $10^{16}$ | $\approx 0$ | 6.9 | |
| | .445 | 1.7 | 7.0 | 2360 | 1510 | 1.56 |
| 3.5 | .36 | .2 | .118 | 52.5 | 31.2 | 1.68 |
| | .54 | .089 | .165 | 49 | 35.3 | 1.40 |
| 6.0 | 0 | -.093 | .015 | 0 | 20.4 | |
| | .54 | -0.71 | 1.49 | -605 | 1160 | 0.52 |
| 10.0 | 0 | -.023 | .0013 | 0 | -2.27 | |
| | .54 | .157 | .092 | 130 | 195 | .667 |

## Table IV

### DOMINANT FREQUENCIES

| Source Location | | Dominant Frequency $f_L$ | | |
|---|---|---|---|---|
| $y_1/D$ | r/D | Shear Noise | Self Noise | Overall |
| 3.5 | 0.54 | | | |
| 4.0 | .54 | 1000 | 2000 | |
| 5.0 | .54 | 925 | 1800 | |
| 6.0 | .54 | 1600 | 2700 | 2200 |
| 7.0 | .54 | 1200 | 2200 | |
| 10.0 | 0 | 900 | 1500 | 1400 |

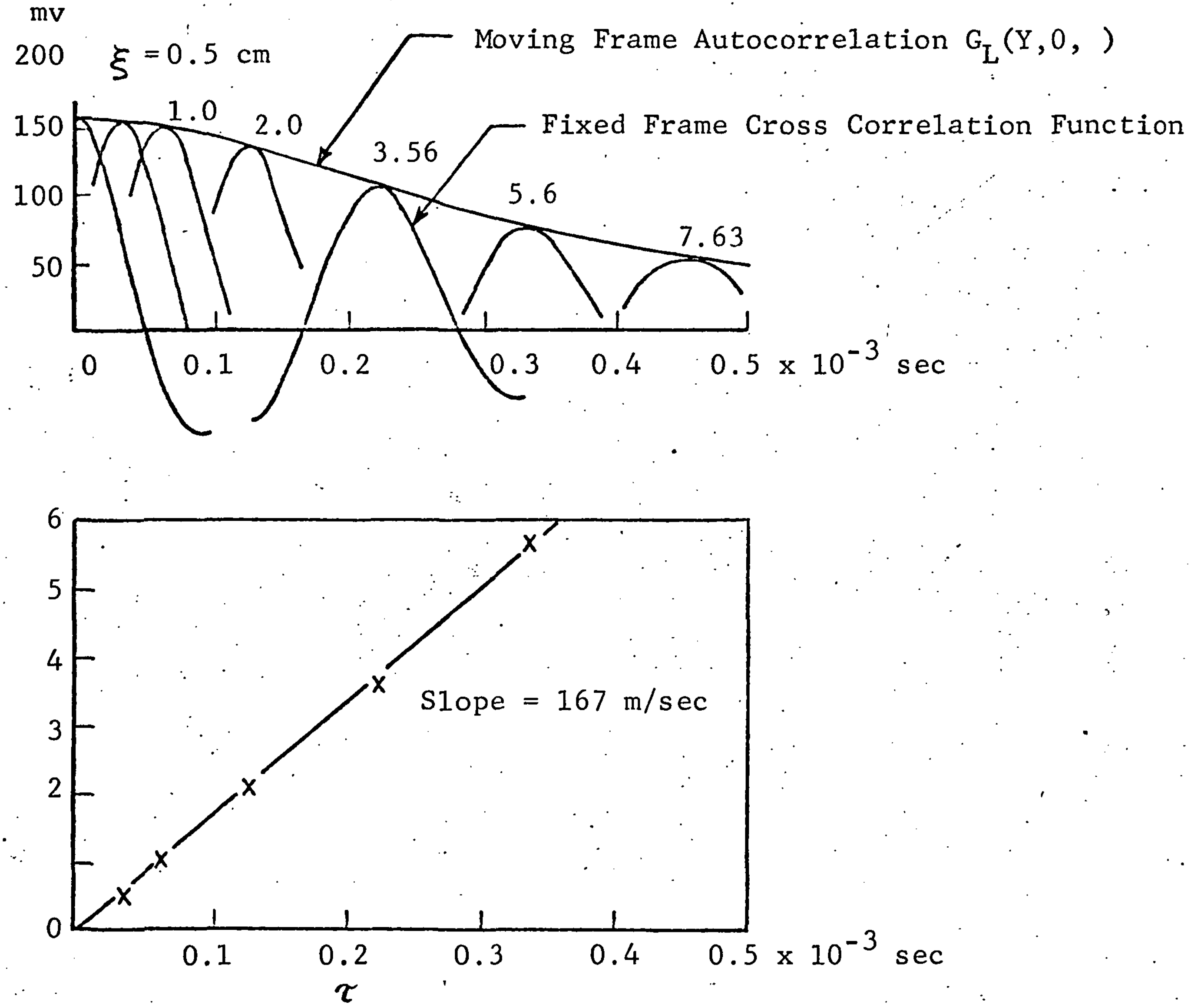

Figure 1 Space-Time Correlations

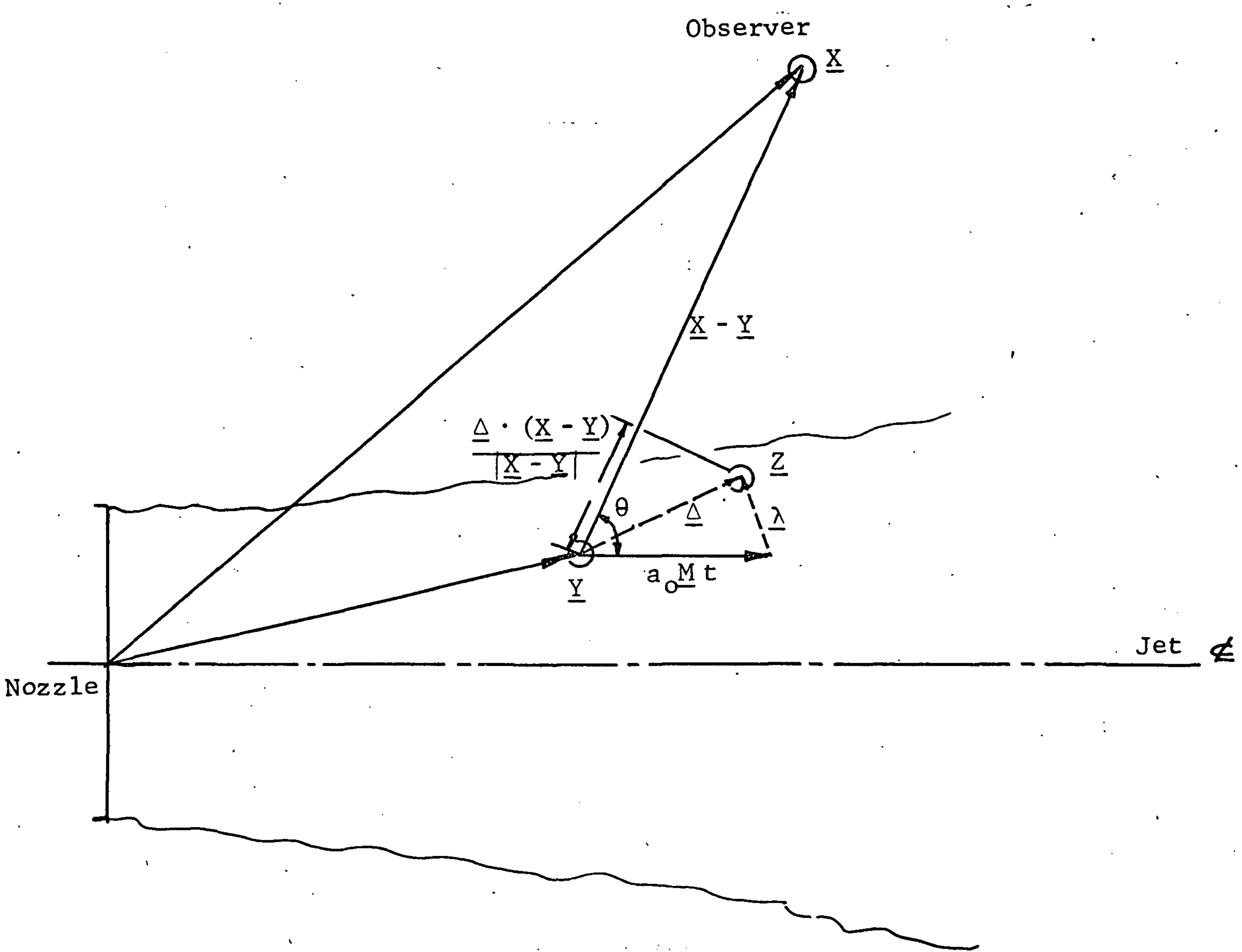

Figure 2 Coordinate Axes System

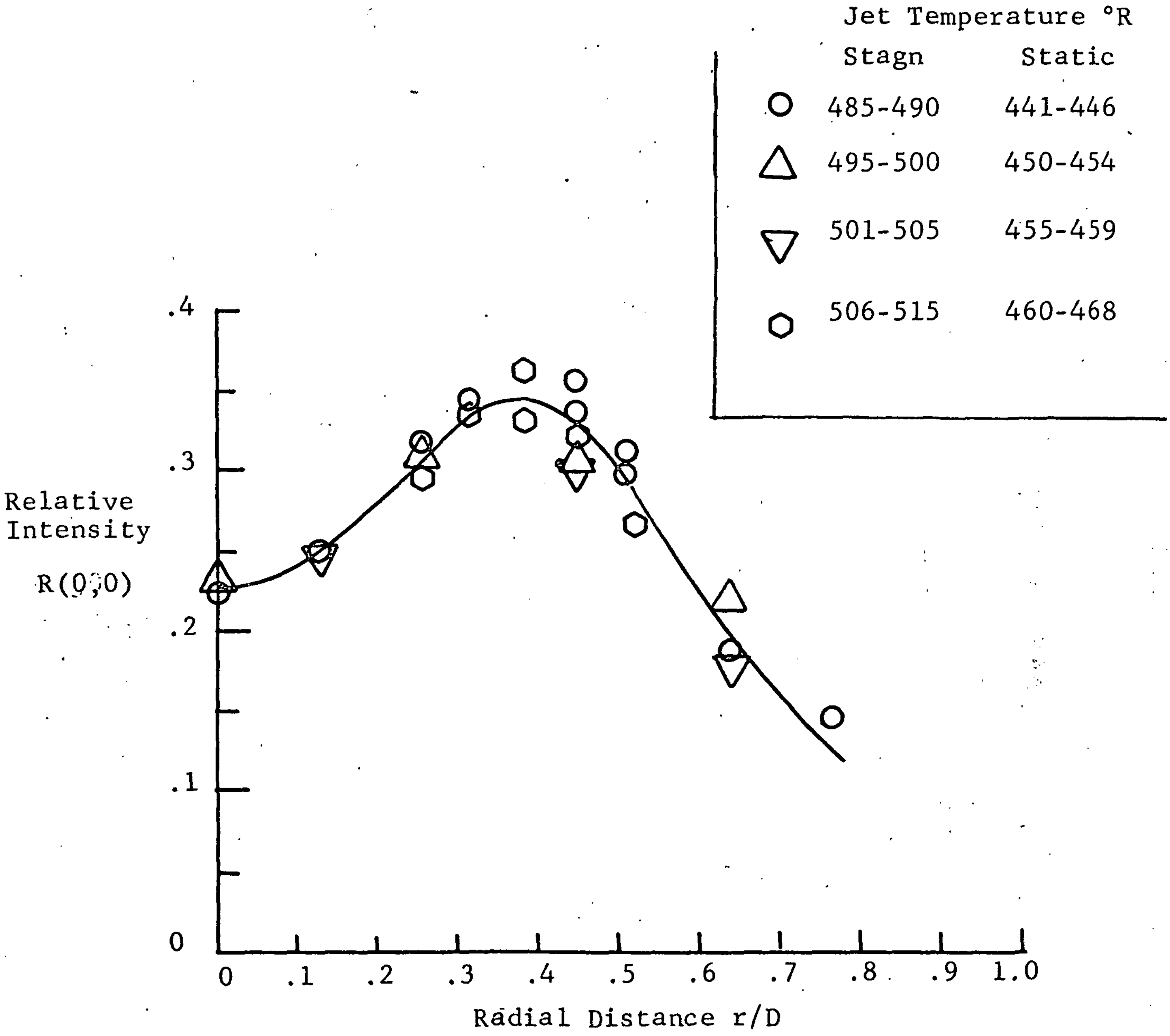

Figure 3 Effect of Jet Temperature on Measured Intensity. Jet Velocity - 235 m/sec, $y_1/D = 2$

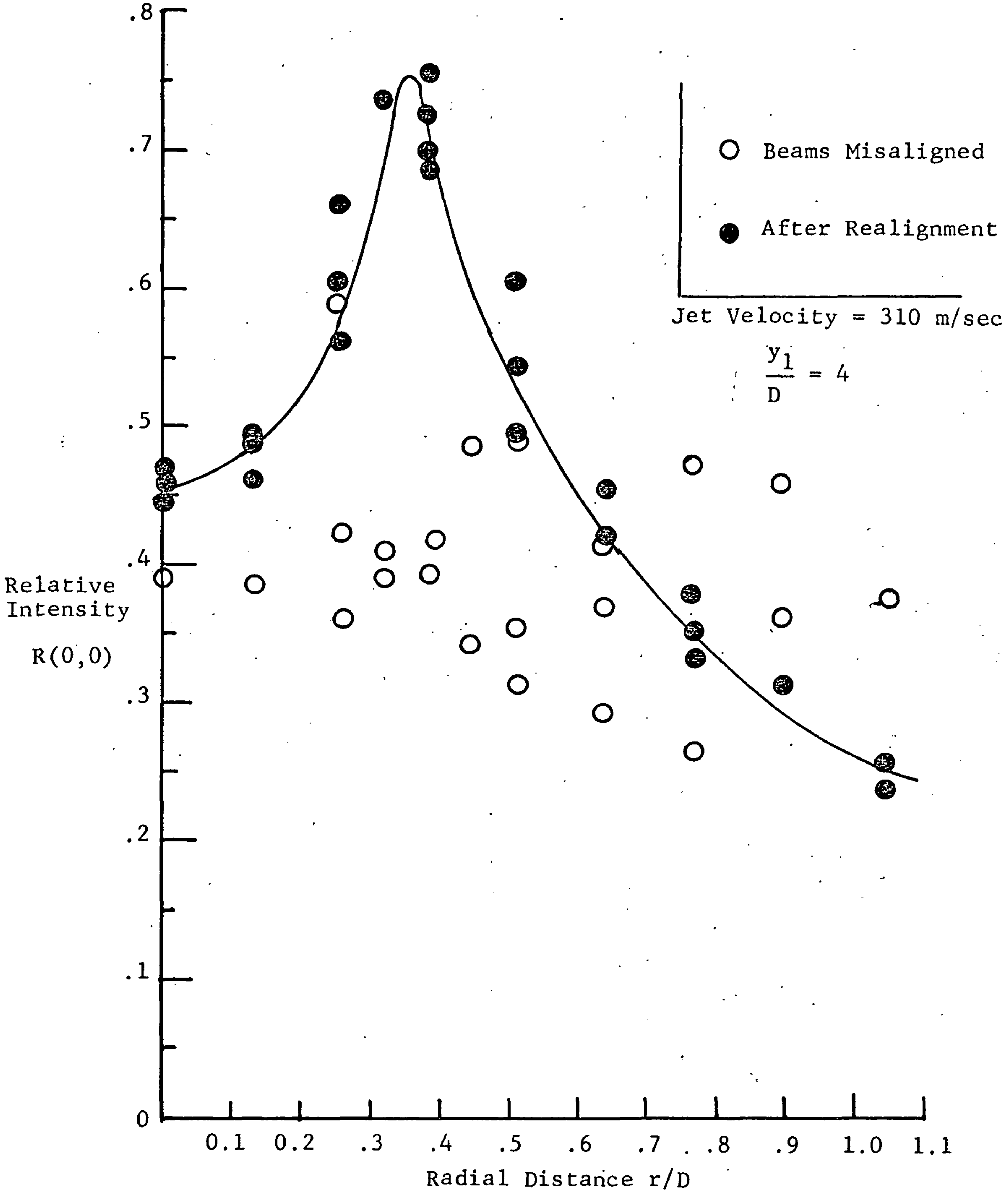

Figure 4 Effect of Beam Misalignment

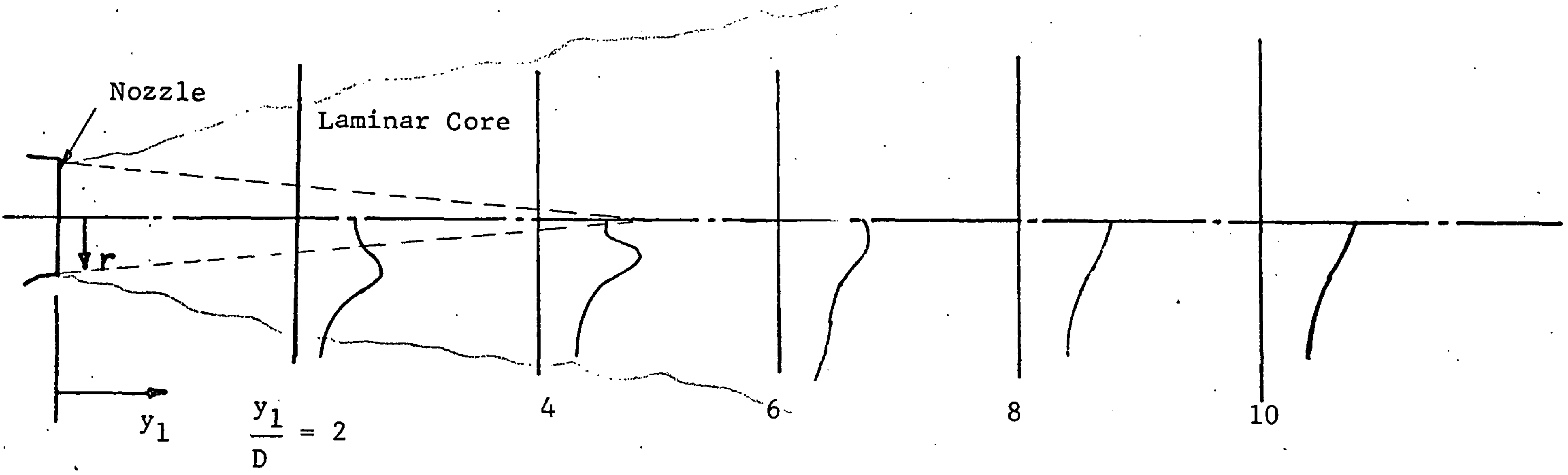

Figure 5 Relative Intensity Profiles - M = 1 Jet

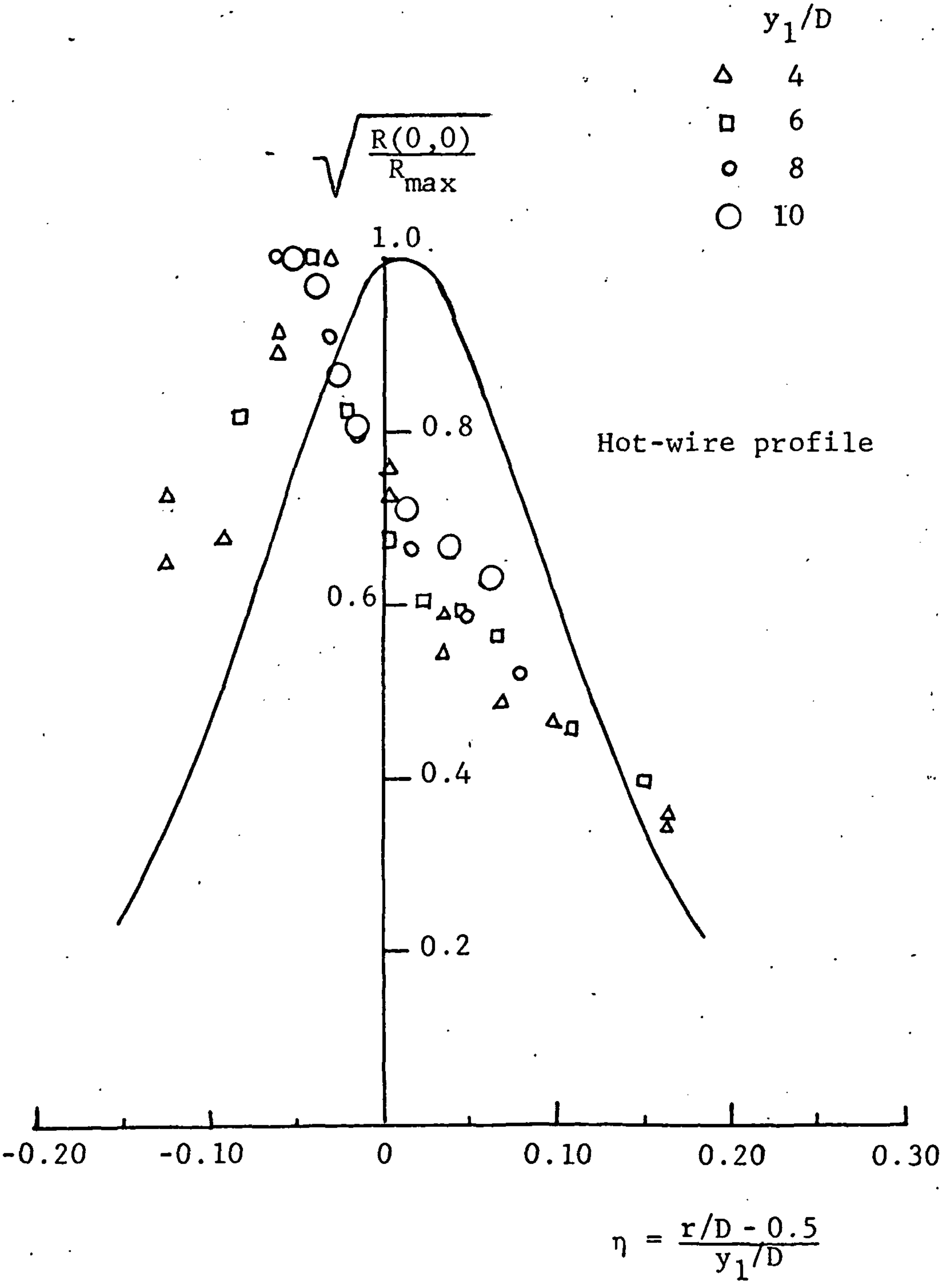

Figure 6 Normalized Intensity Profiles Measured by the Crossed Beams at 4.31 microns. Jet Velocity 315 m/sec

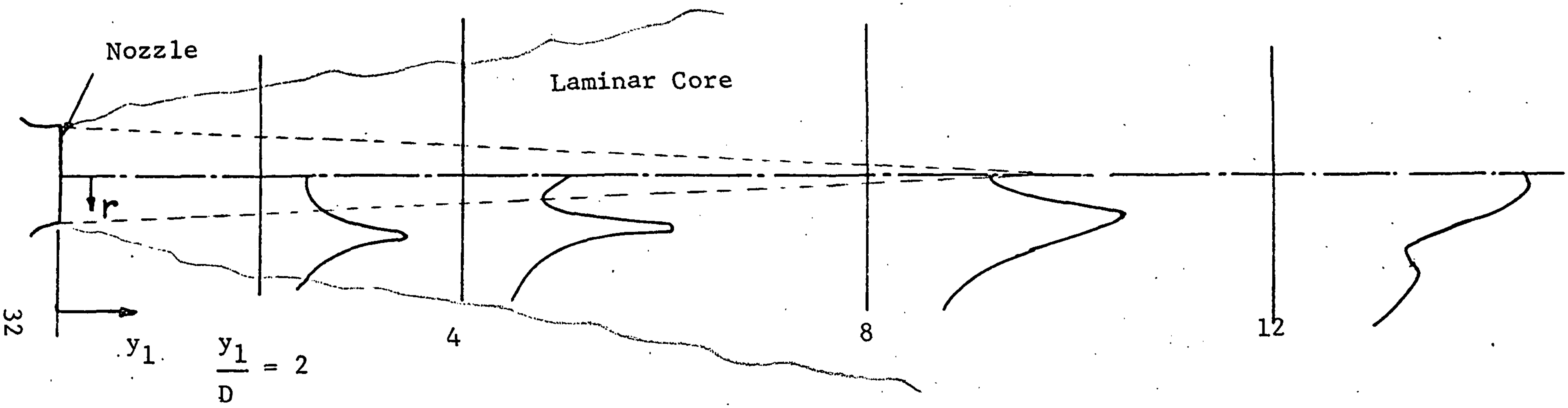

Figure 7 Relative Intensity Profiles - Supersonic Jet at M = 1.94

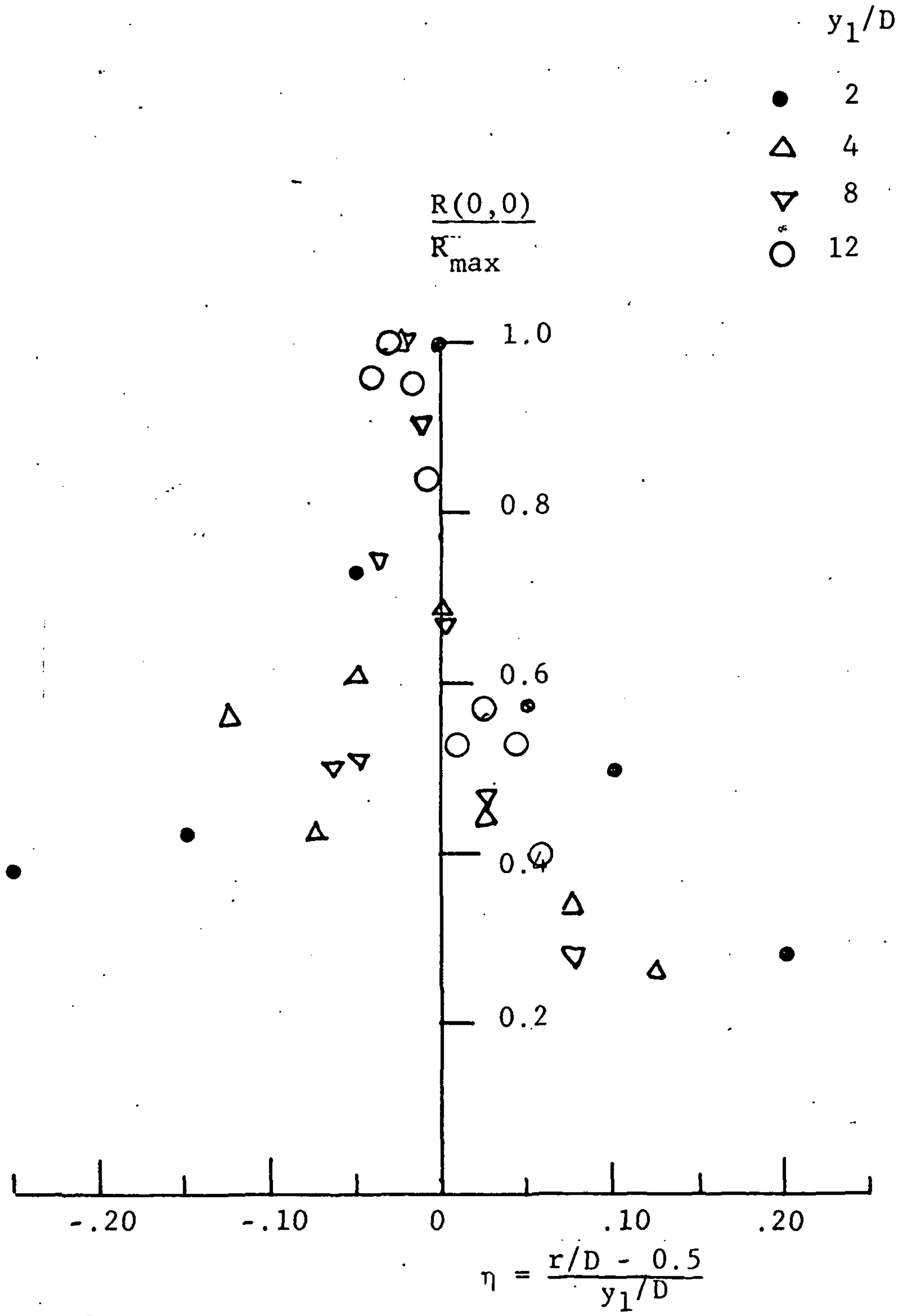

Figure 8 Normalized Intensity Profiles Measured by the Crossed Beams at 4.31 microns. Jet Velocity 485 m/sec (M=1.94)

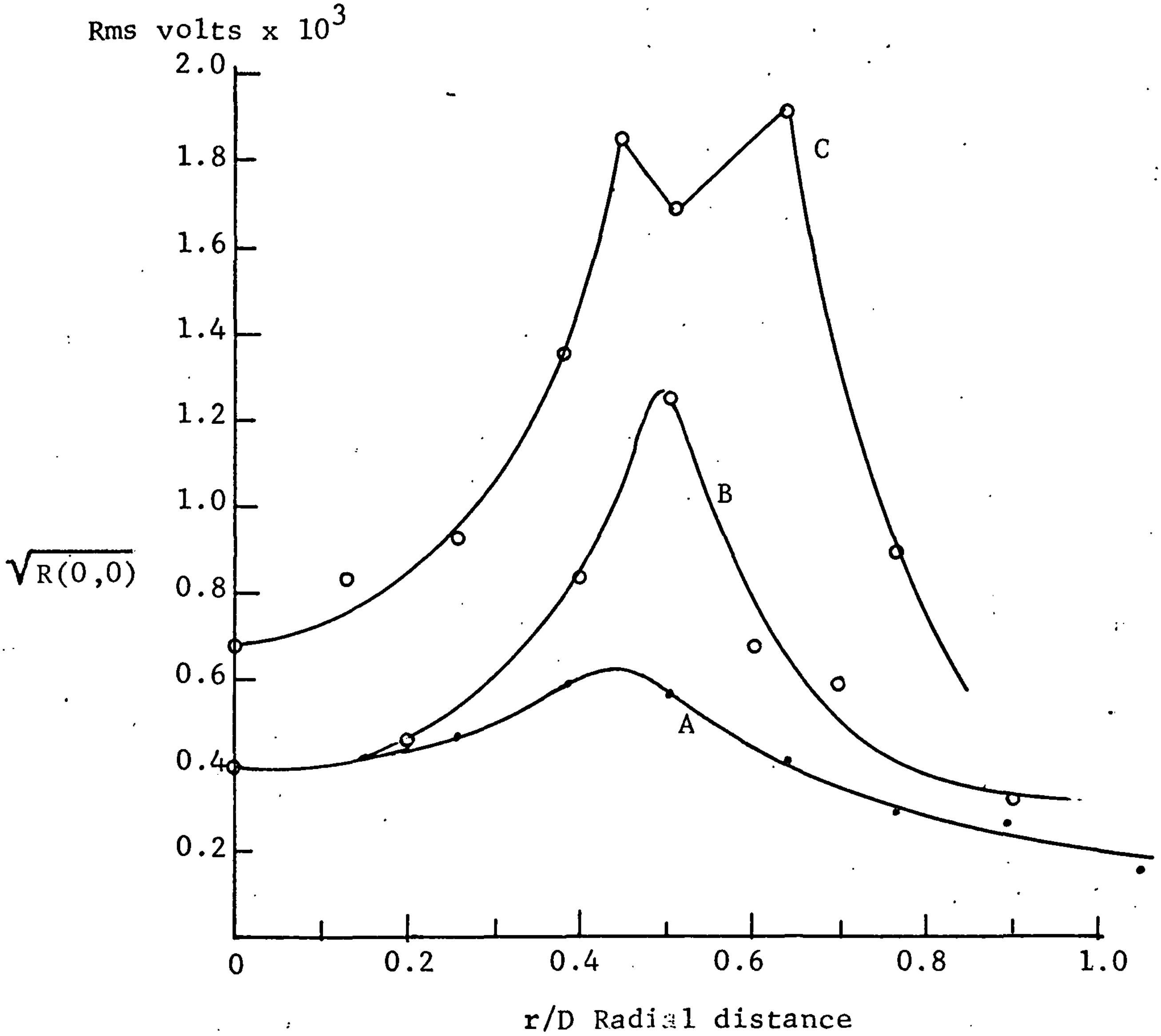

Figure 9 Relative Intensity Profiles for Convergent Nozzle at Three Jet Speeds, $y_1/D=2$
A: 235 m/sec; B: 315 m/sec; C: 485 m/sec

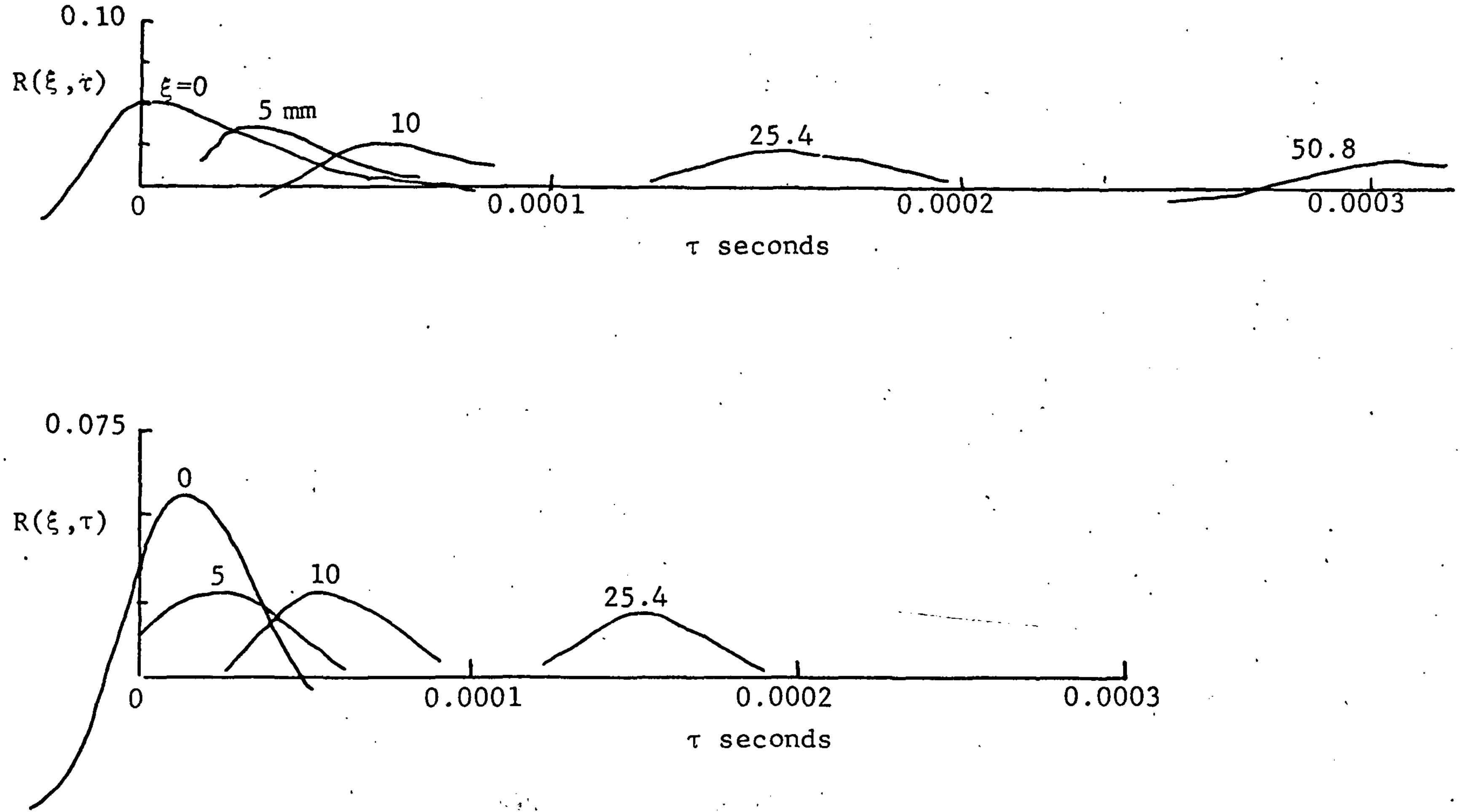

Figure 10 Space-time Correlations - Jet Velocity 235 m/sec
$y_1/D=2$; r=8.9 mm

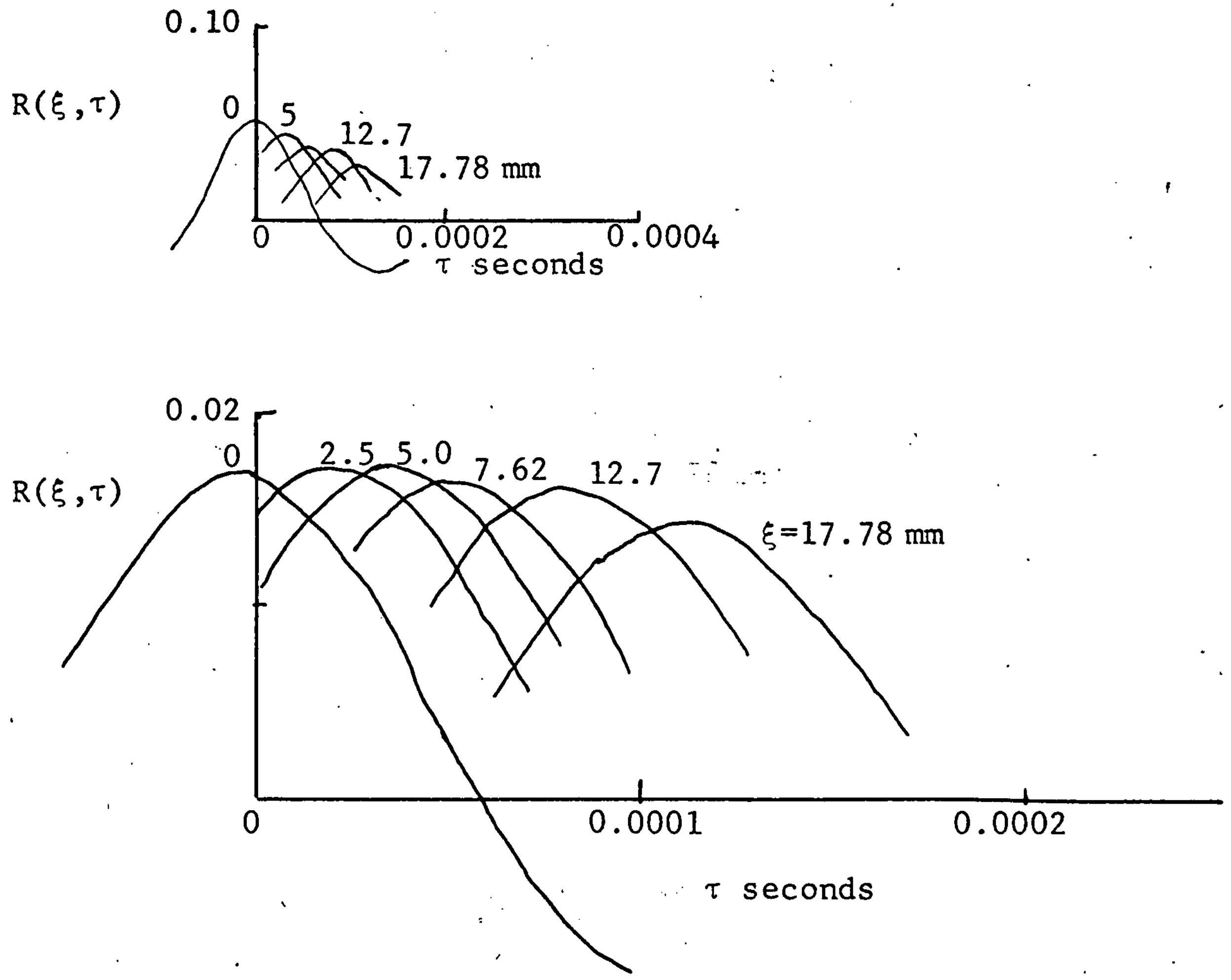

Figure 11 Space-time Correlations - Jet Velocity 235 m/sec
$y_1/D=3.5$; $r=0$

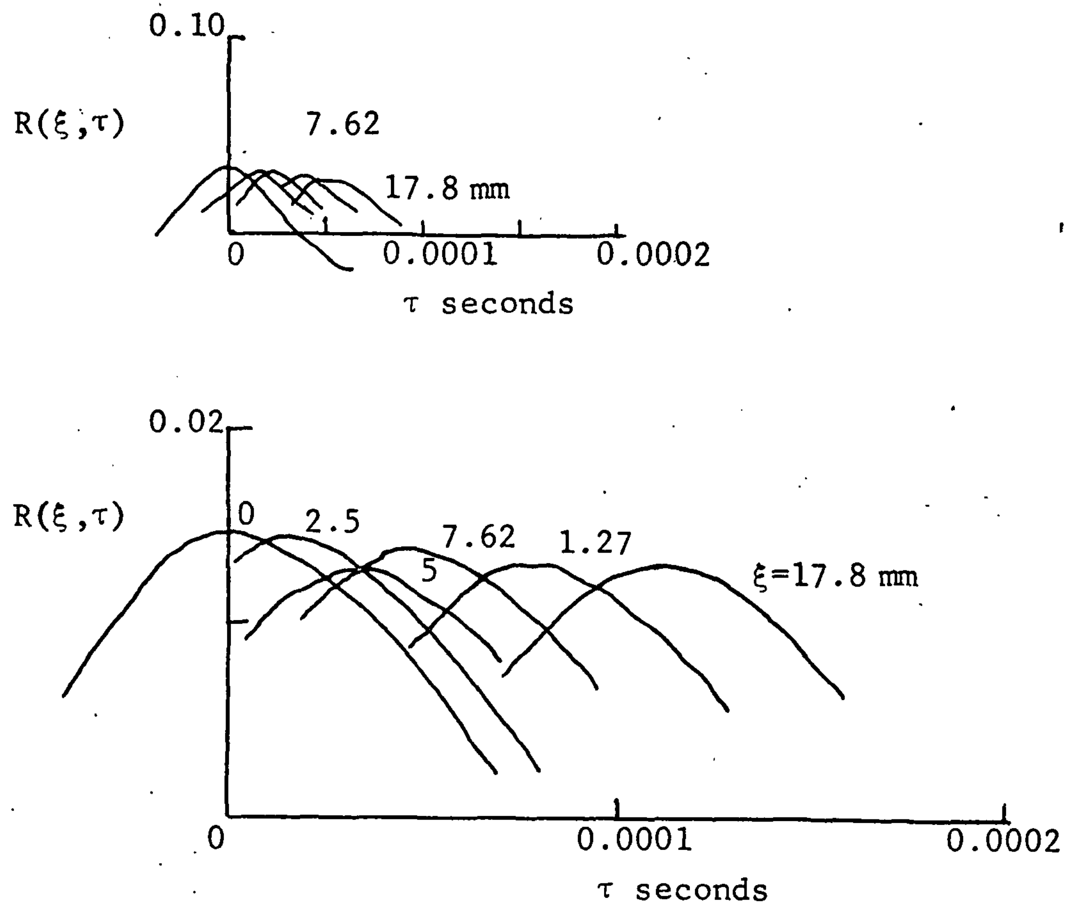

Figure 12 Space-time Correlations - Jet Velocity 235 m/sec $y_1/D=3.5$; $r=3.6$ mm

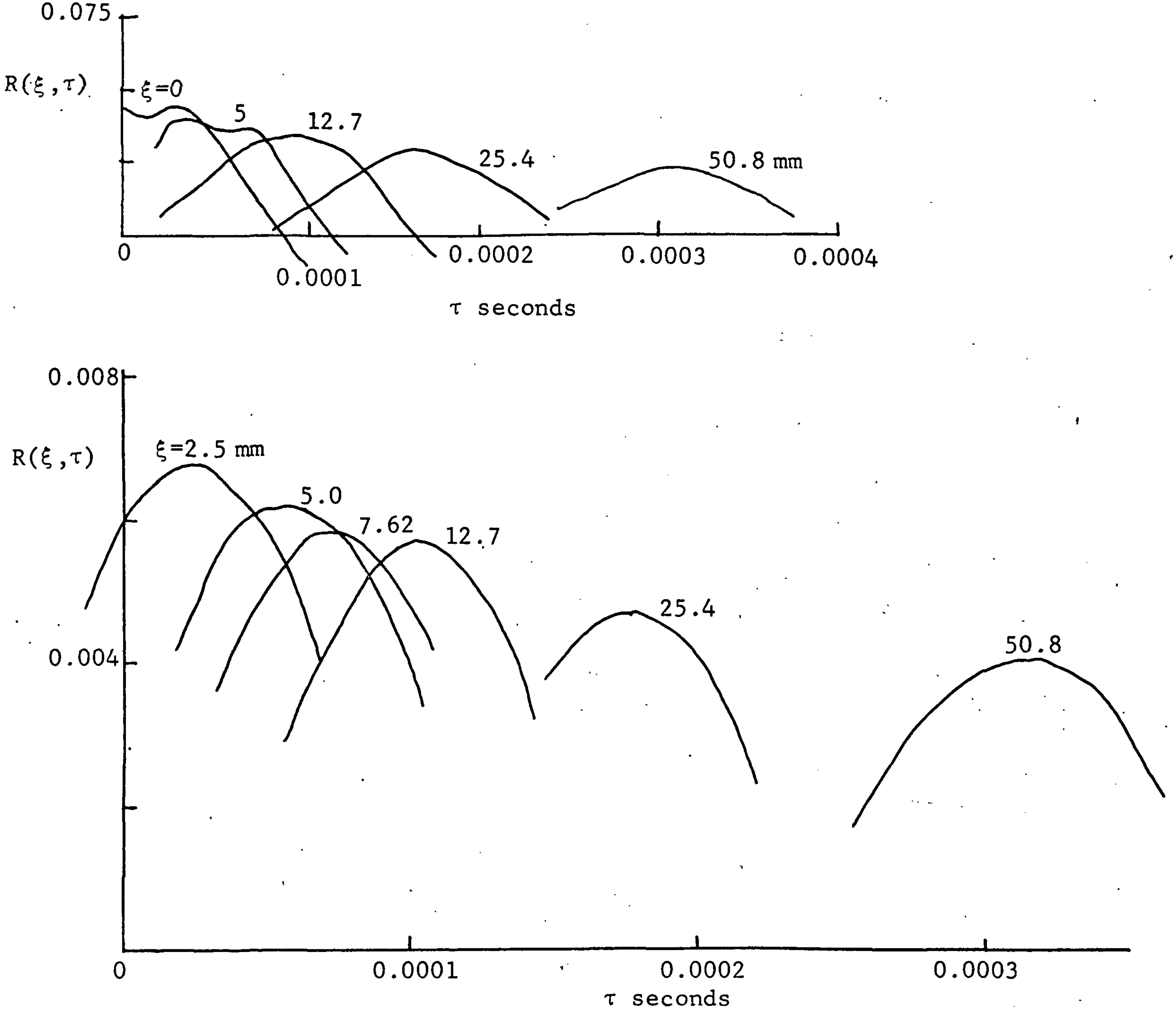

Figure 13 Space-Time Correlations - Jet Velocity 235 m/sec
$y_1/D=3.5$; r=10.8 mm

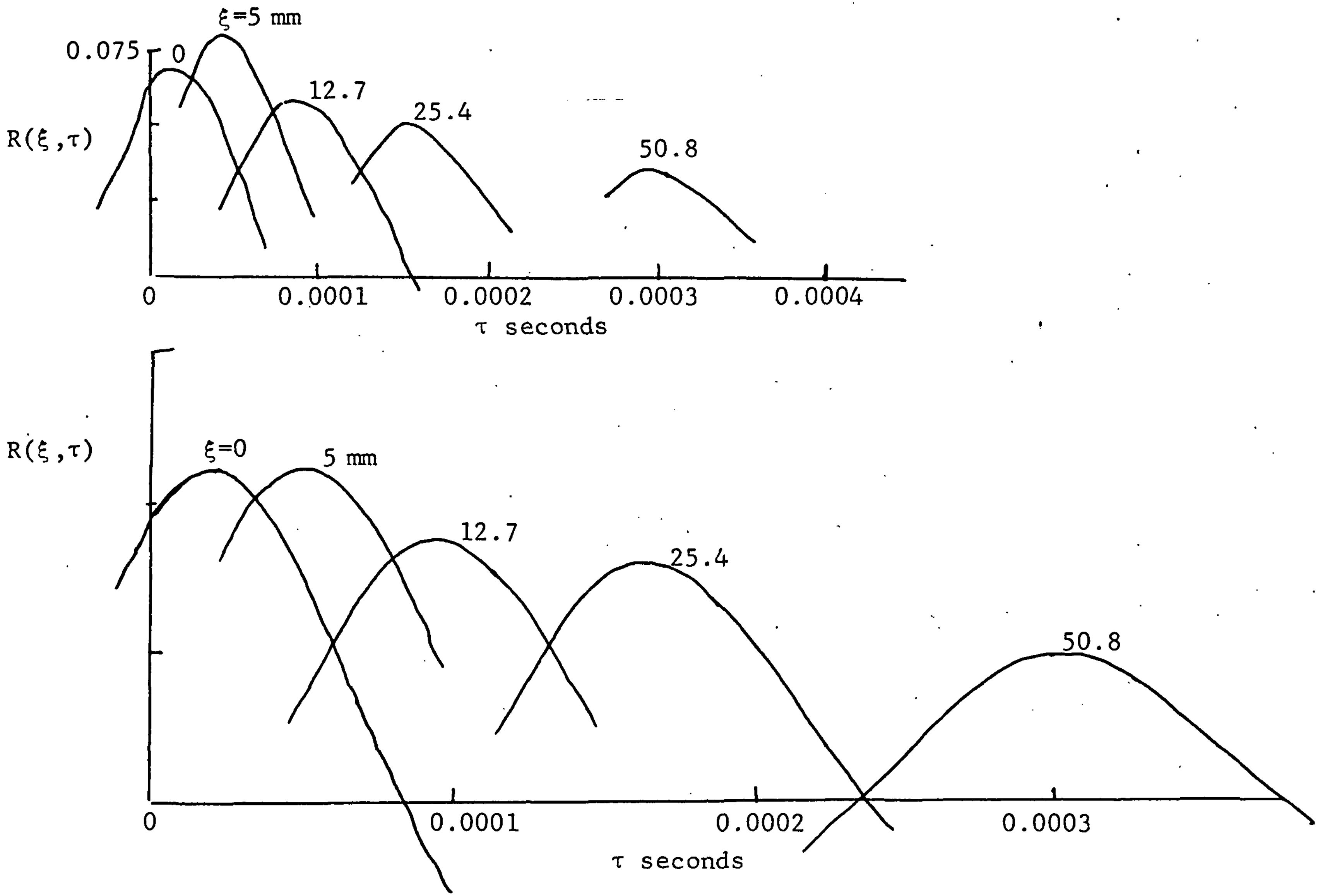

Figure 14 Space-time Correlations - Jet Velocity 235 m/sec
$y_1/D=4.0$; r=10.8 mm

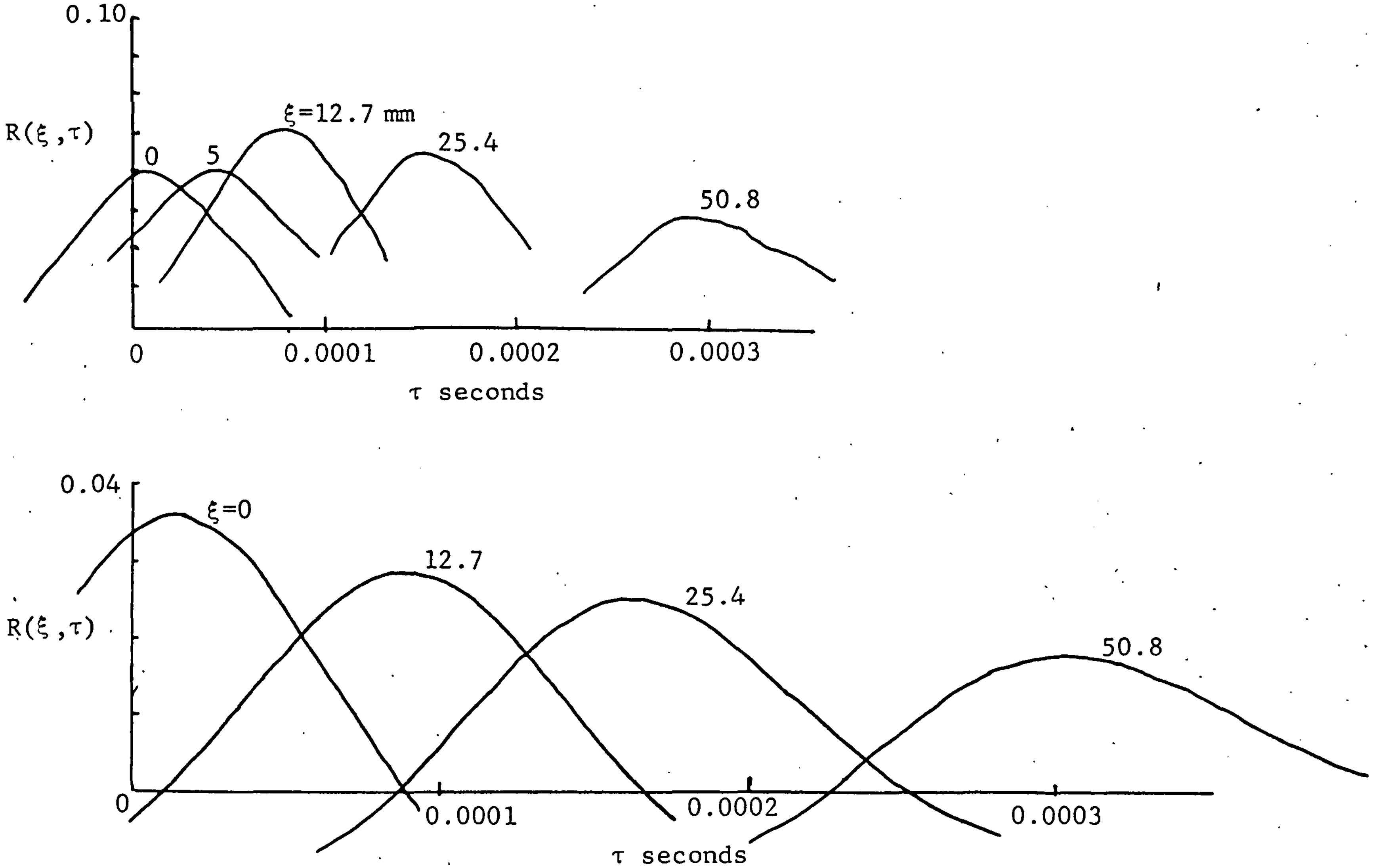

Figure 15 Space-time Correlations - Jet Velocity 235 m/sec $y_1/D=5.0$; r=10.8 mm

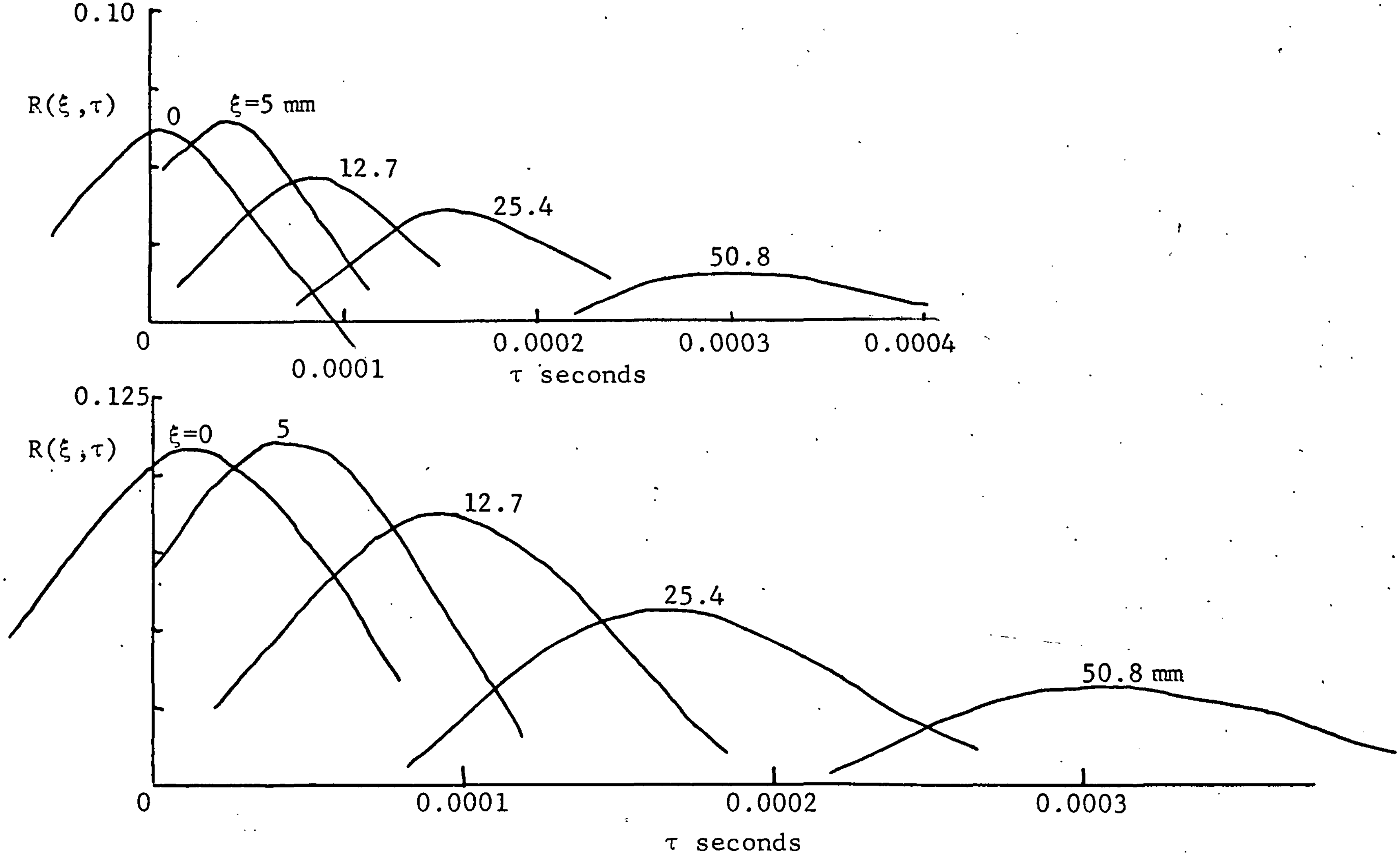

Figure 16 Space-time Correlations - Jet Velocity 235 m/sec
$y_1/D=6.0$; r=10.8 mm

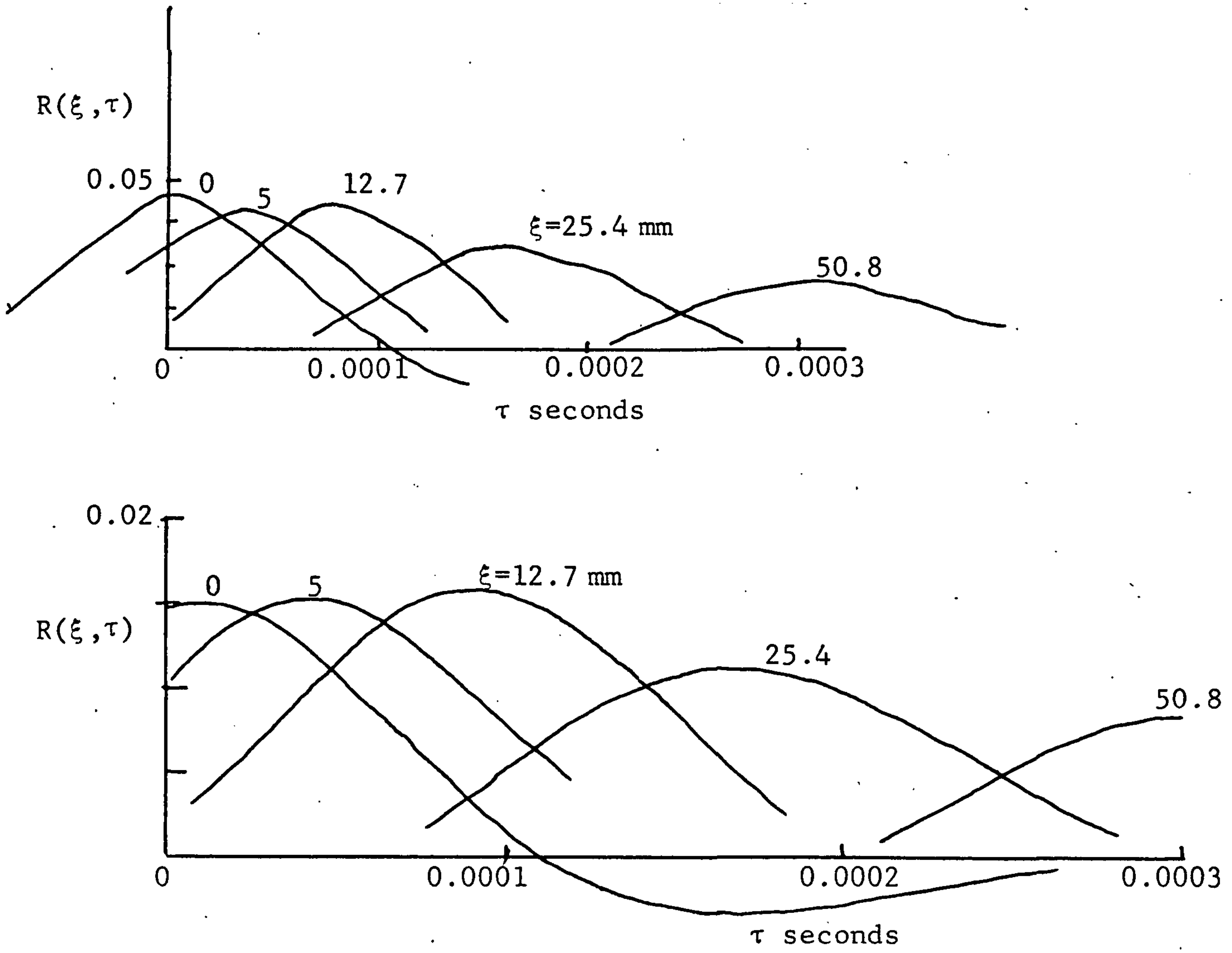

Figure 17 Space-time Correlations - Jet Velocity 235 m/sec
$y_1/D=7.0$; r=10.8 mm

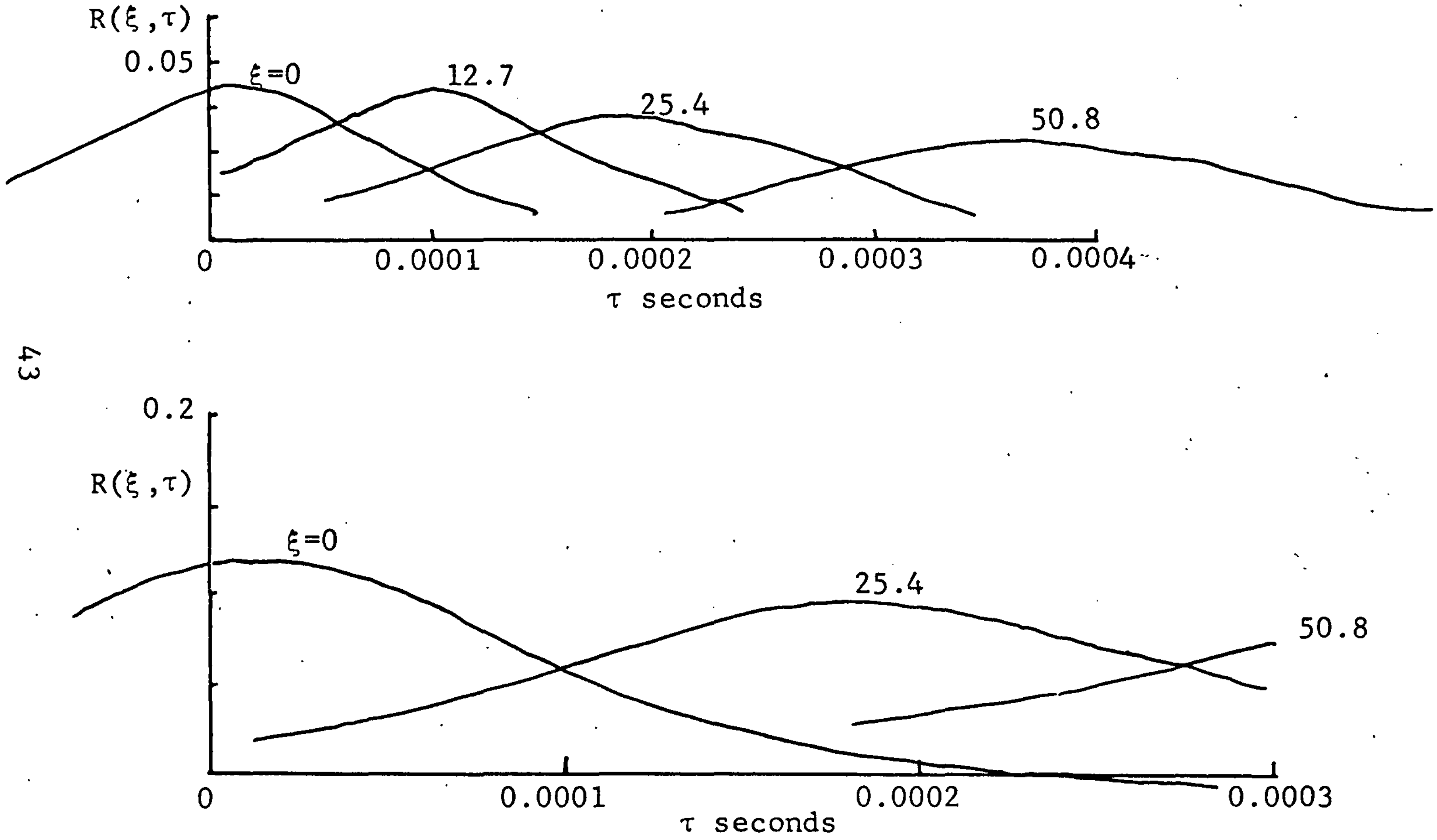

Figure 18 Space-time Correlations - Jet Velocity 235 m/sec
$y_1/D=10$; r=0

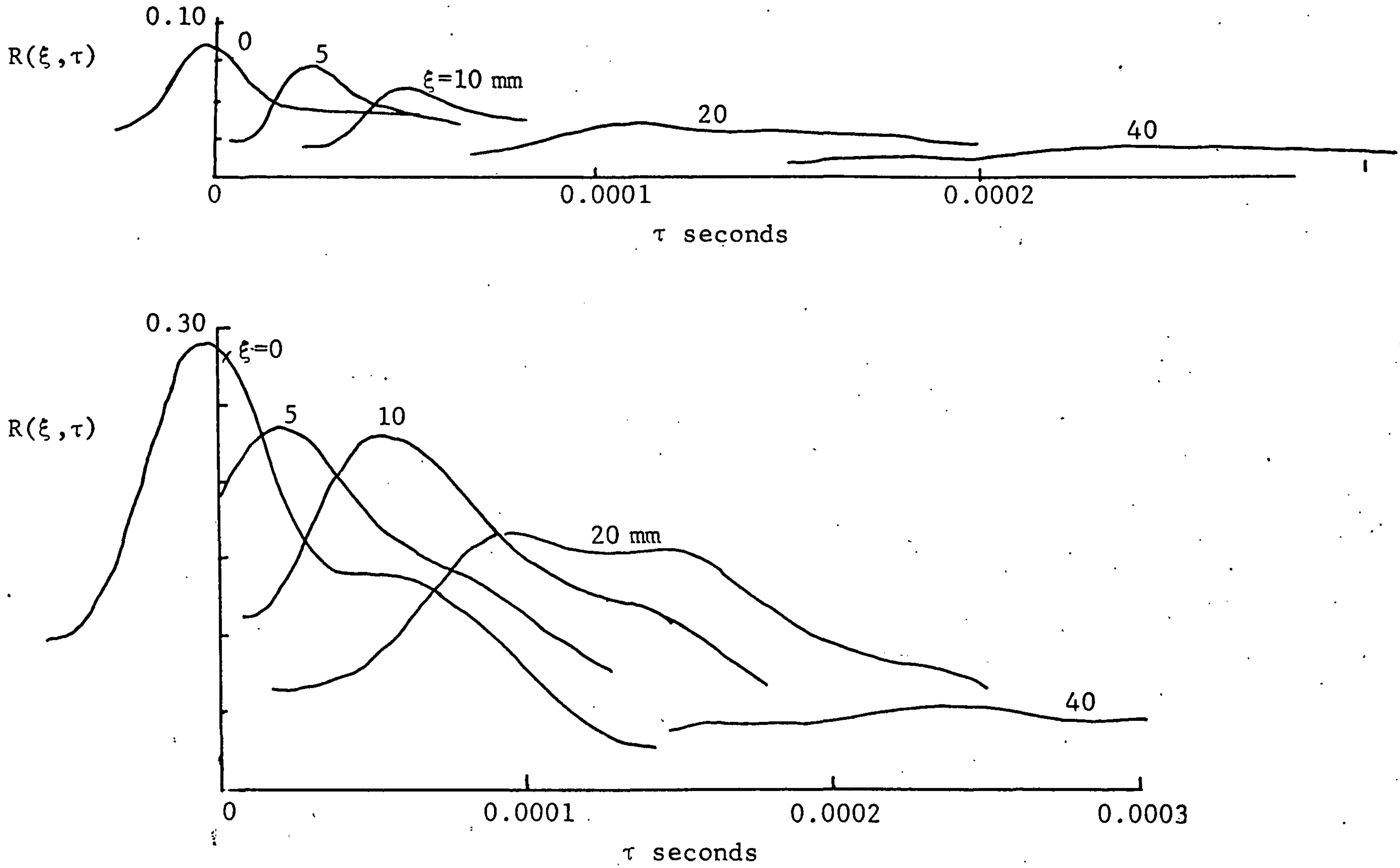

Figure 19 Space-time Correlations - Jet Velocity 315 m/sec
$y_1/D=10$; r=5.1 mm

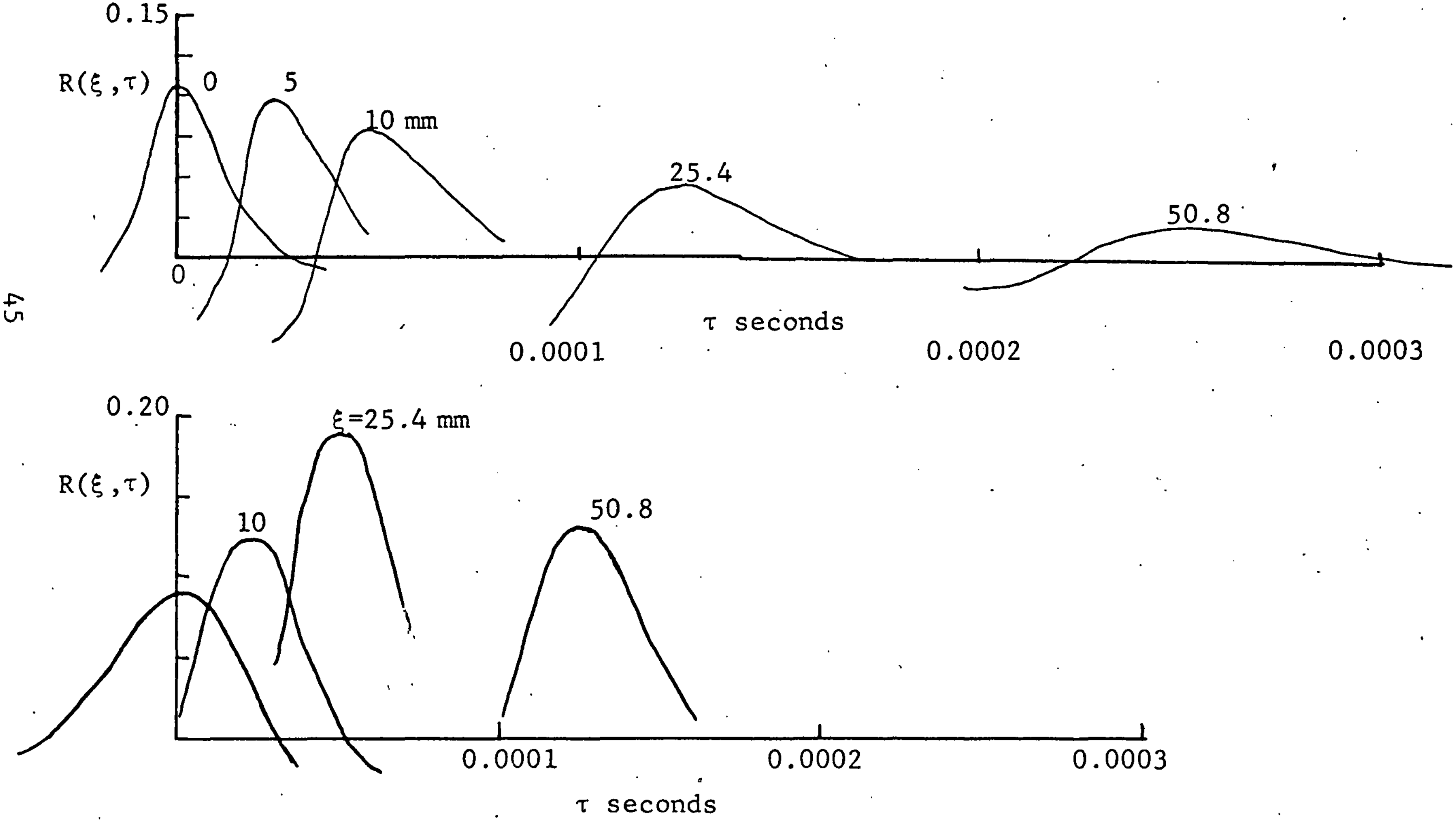

Figure 20 Space-time Correlations - Jet Velocity 315 m/sec
$y_1/D=2$; r=7.62 mm

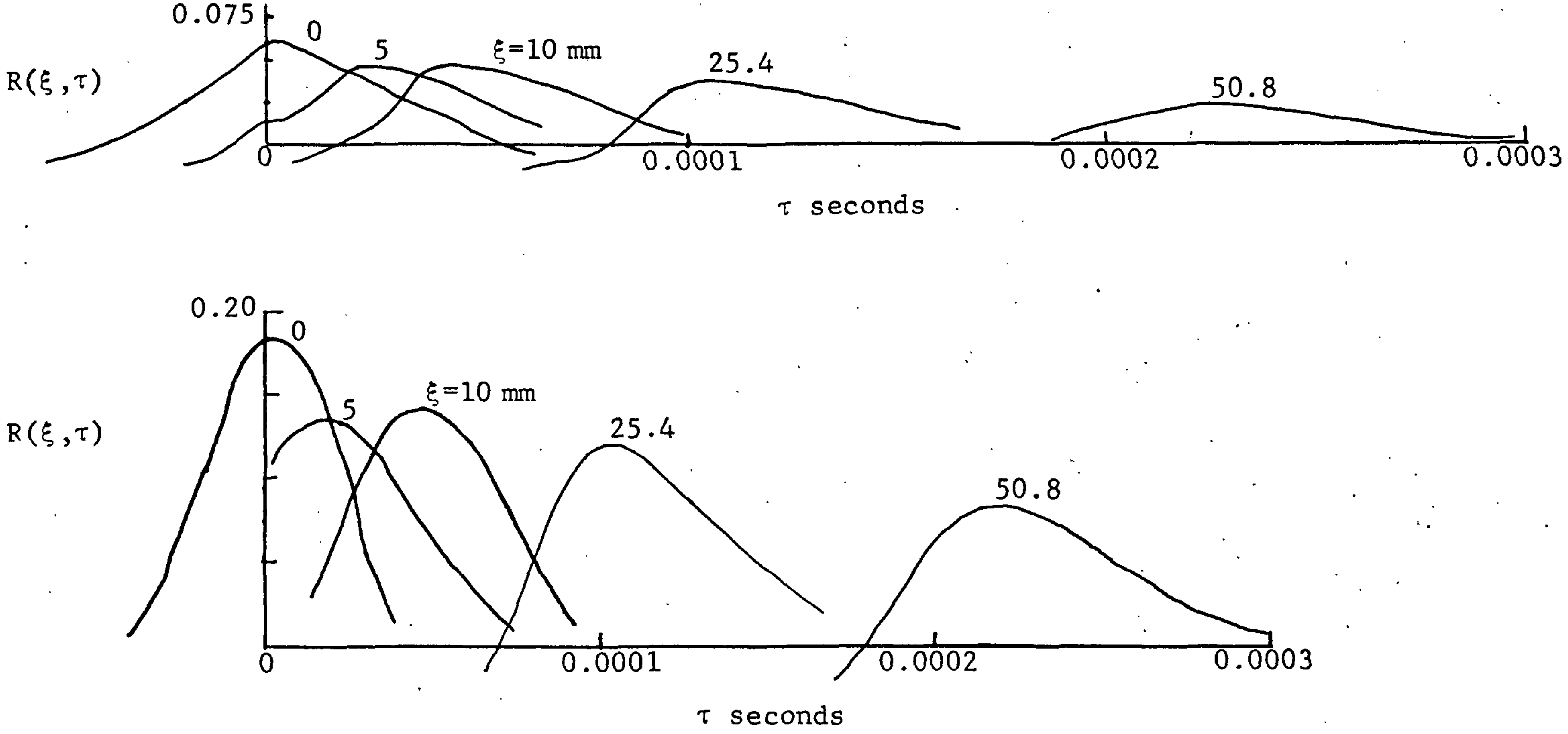

Figure 21 Space-time Correlations - Jet Velocity 315 m/sec
$y_1/D=4$; r=0

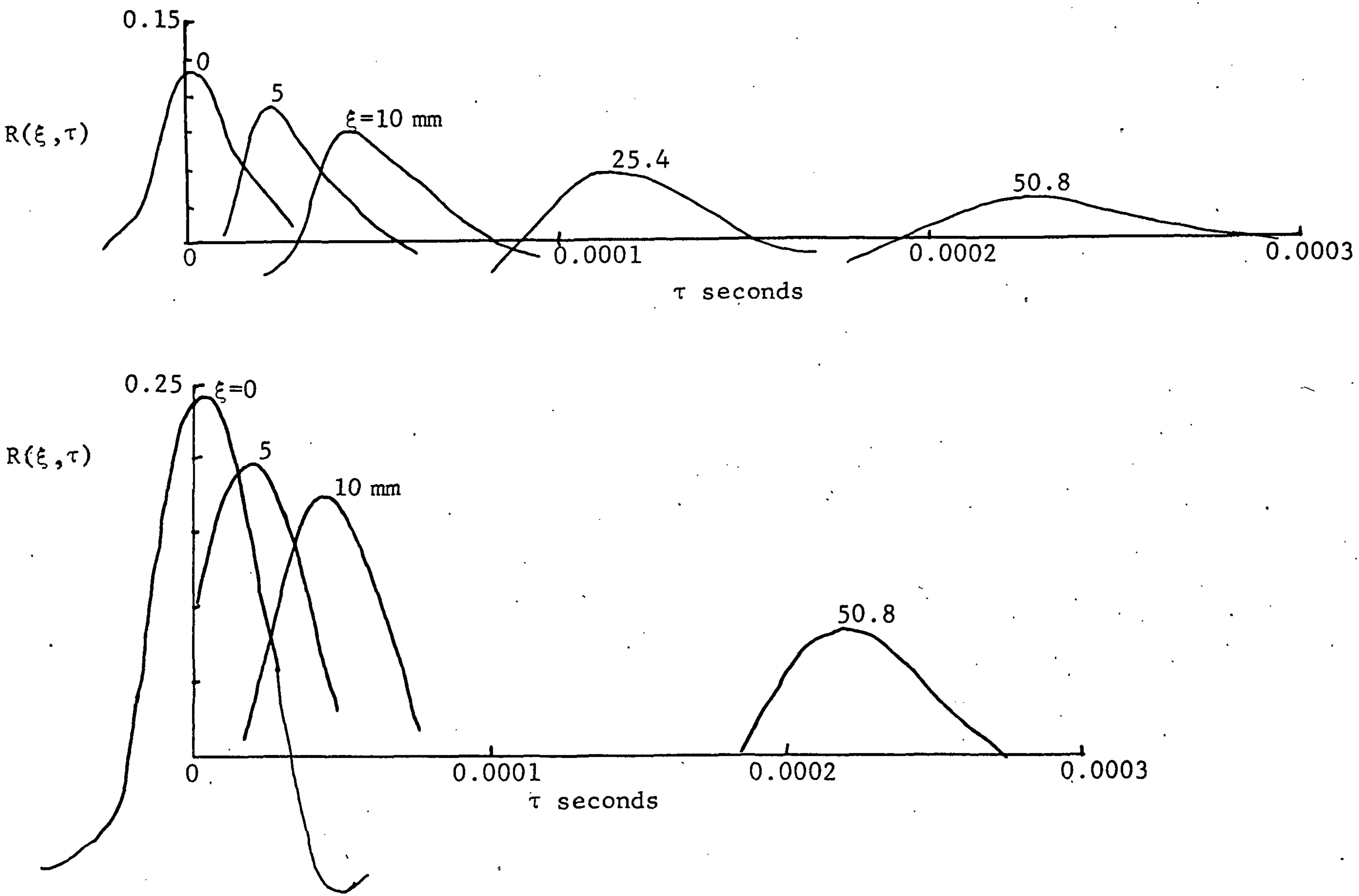

Figure 22 Space-time Correlations - Jet Velocity 315 m/sec
$y_1/D=4$; r=7.62 mm

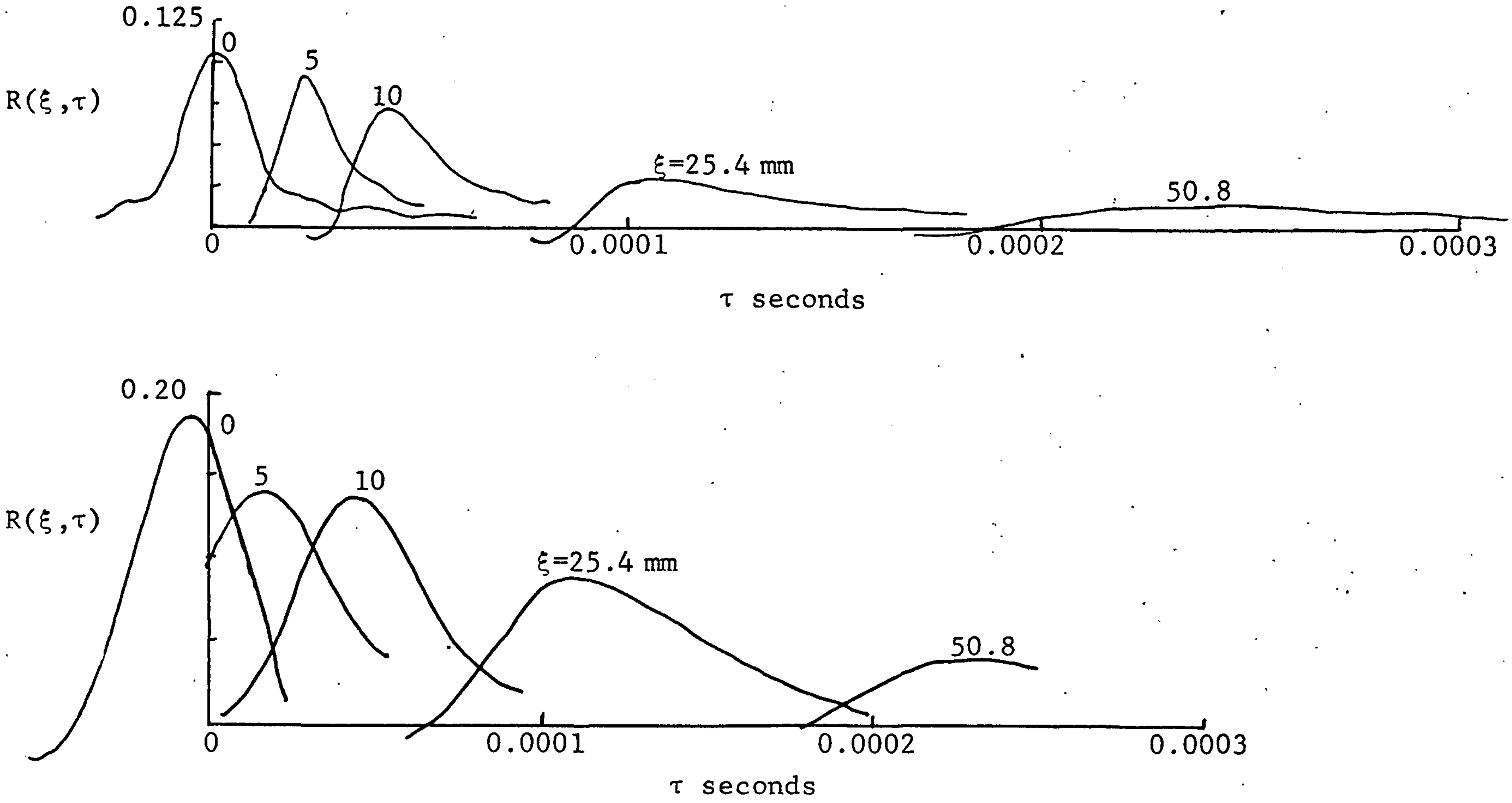

Figure 23 Space-time Correlations - Jet Velocity 315 m/sec
$y_1/D=6$; r=5.08 mm

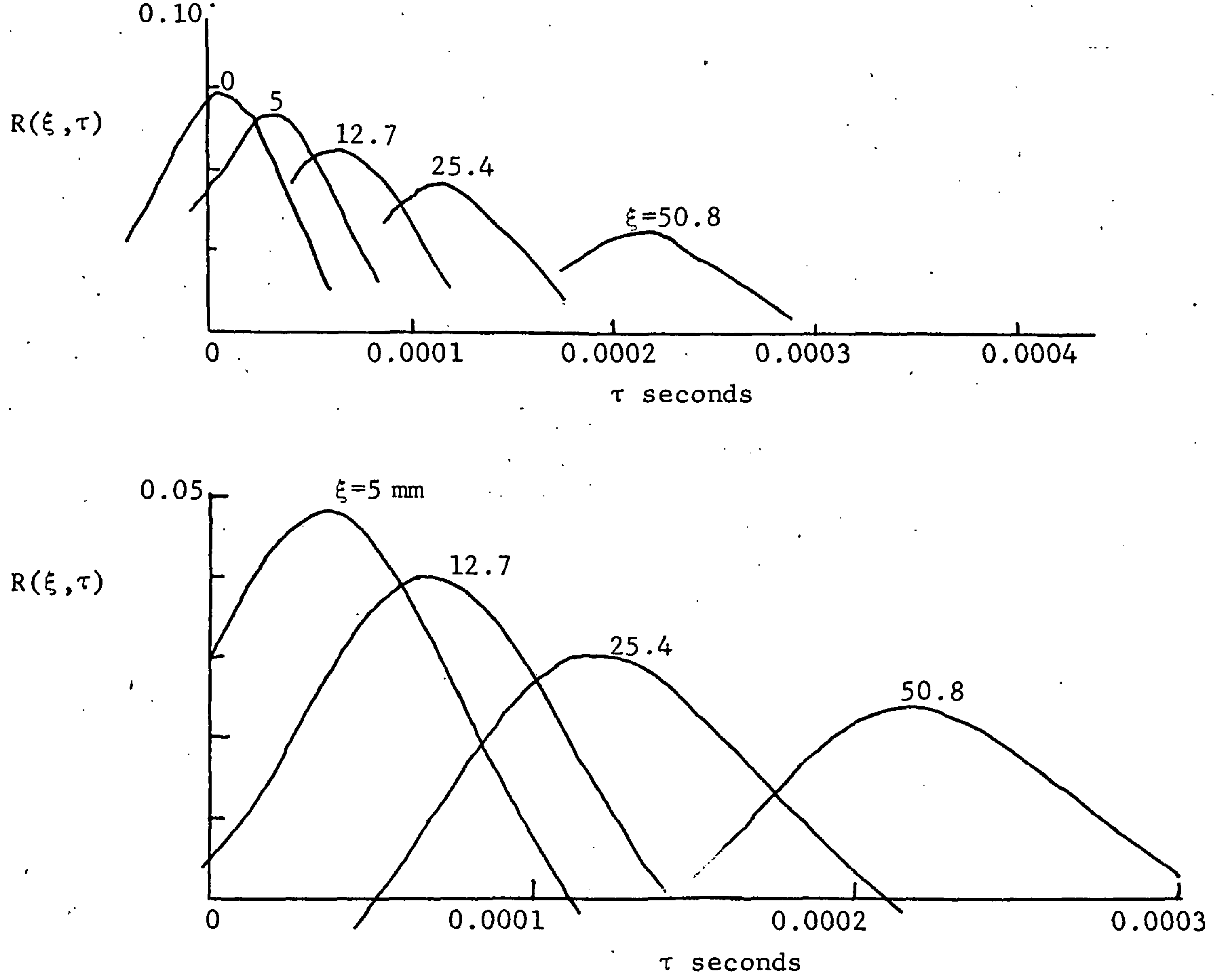

Figure 24 Space-time Correlations - Jet Velocity 315 m/sec
$y_1/D=7$; r=10.8 mm

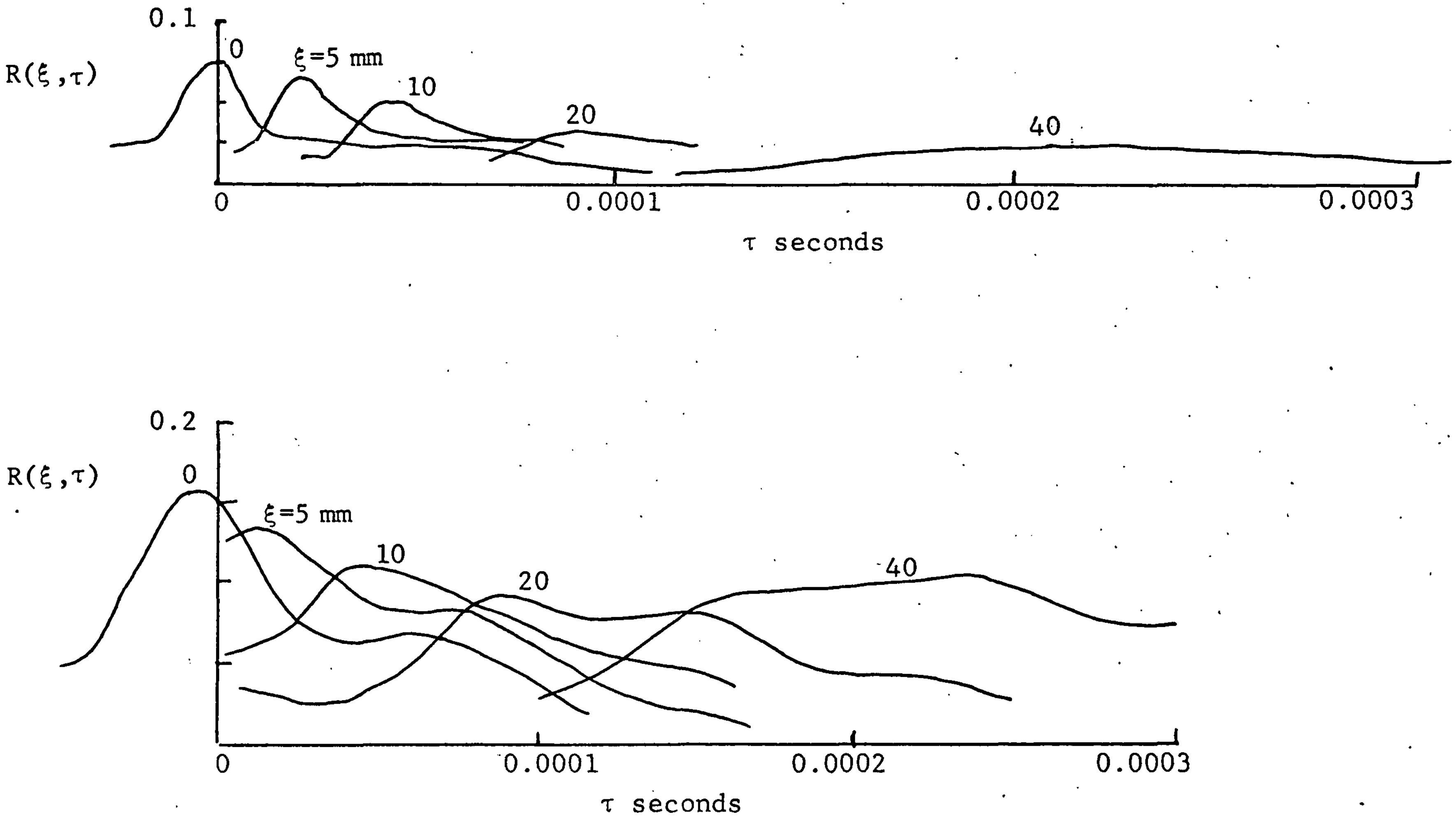

Figure 25 Space-time Correlations - Jet Velocity 315 m/sec
$y_1/D=10$; r=0

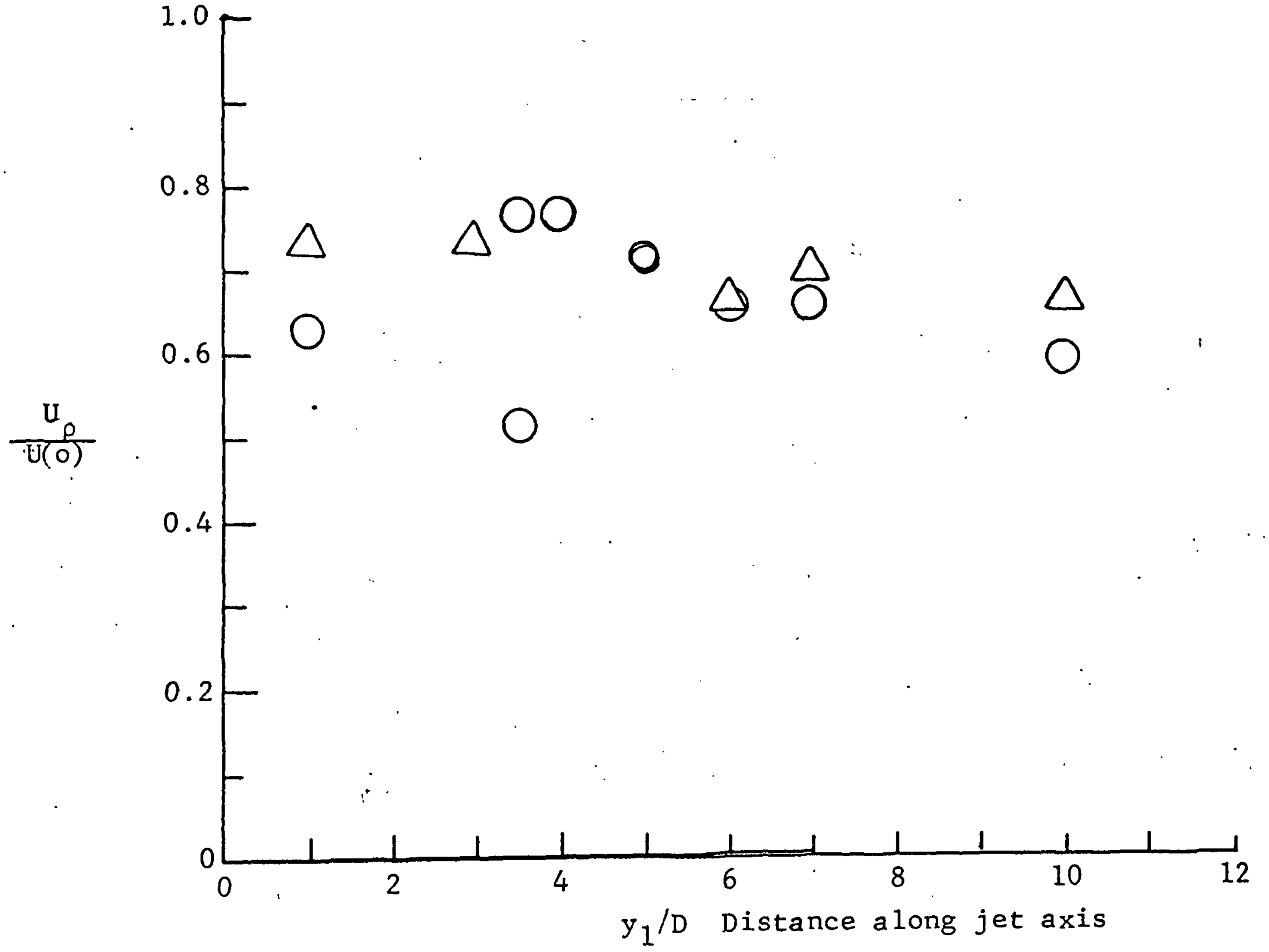

Figure 26 Variation of Convection Speeds with Axial Distance;
O Jet Velocity 235 m/sec; Δ Jet Velocity 315 m/sec

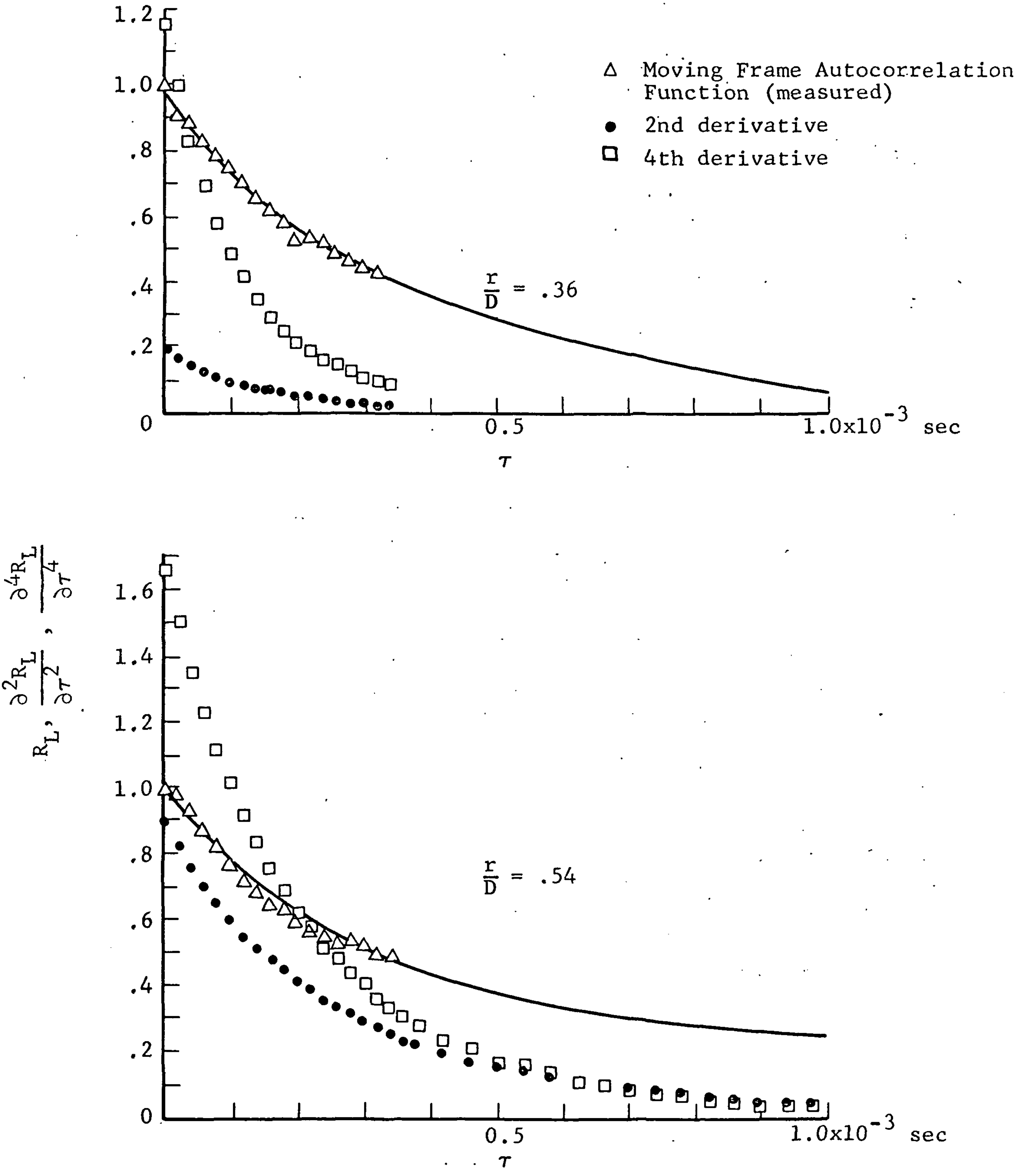

Figure 27 Moving Frame Autocorrelation And Its Derivatives $\frac{y_1}{D} = 3.5$ M = 0.71 Jet

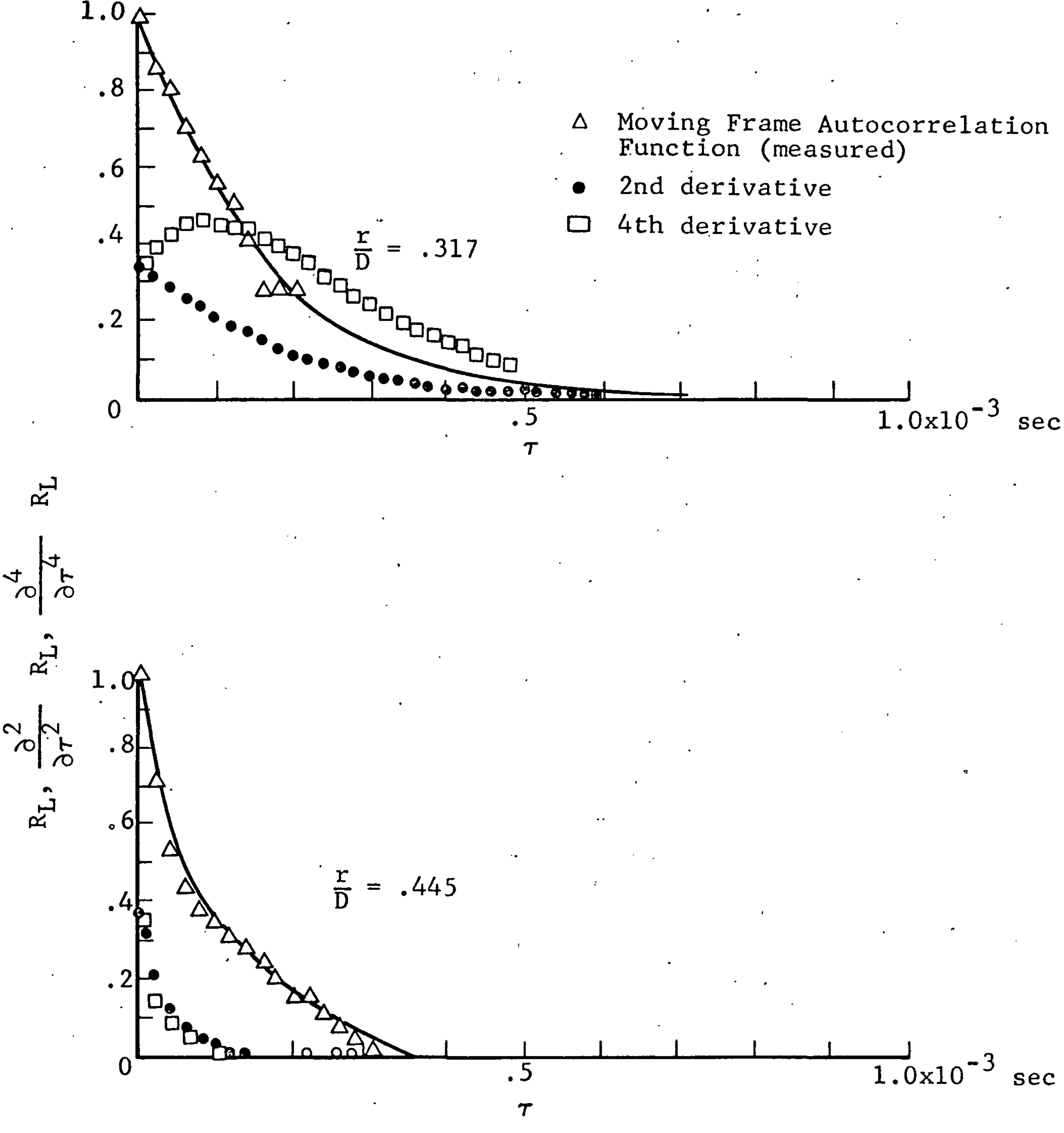

Figure 28   Moving Frame Autocorrelation And Its Derivatives

$\frac{y_1}{D}$ =2.0   M=0.71 Jet

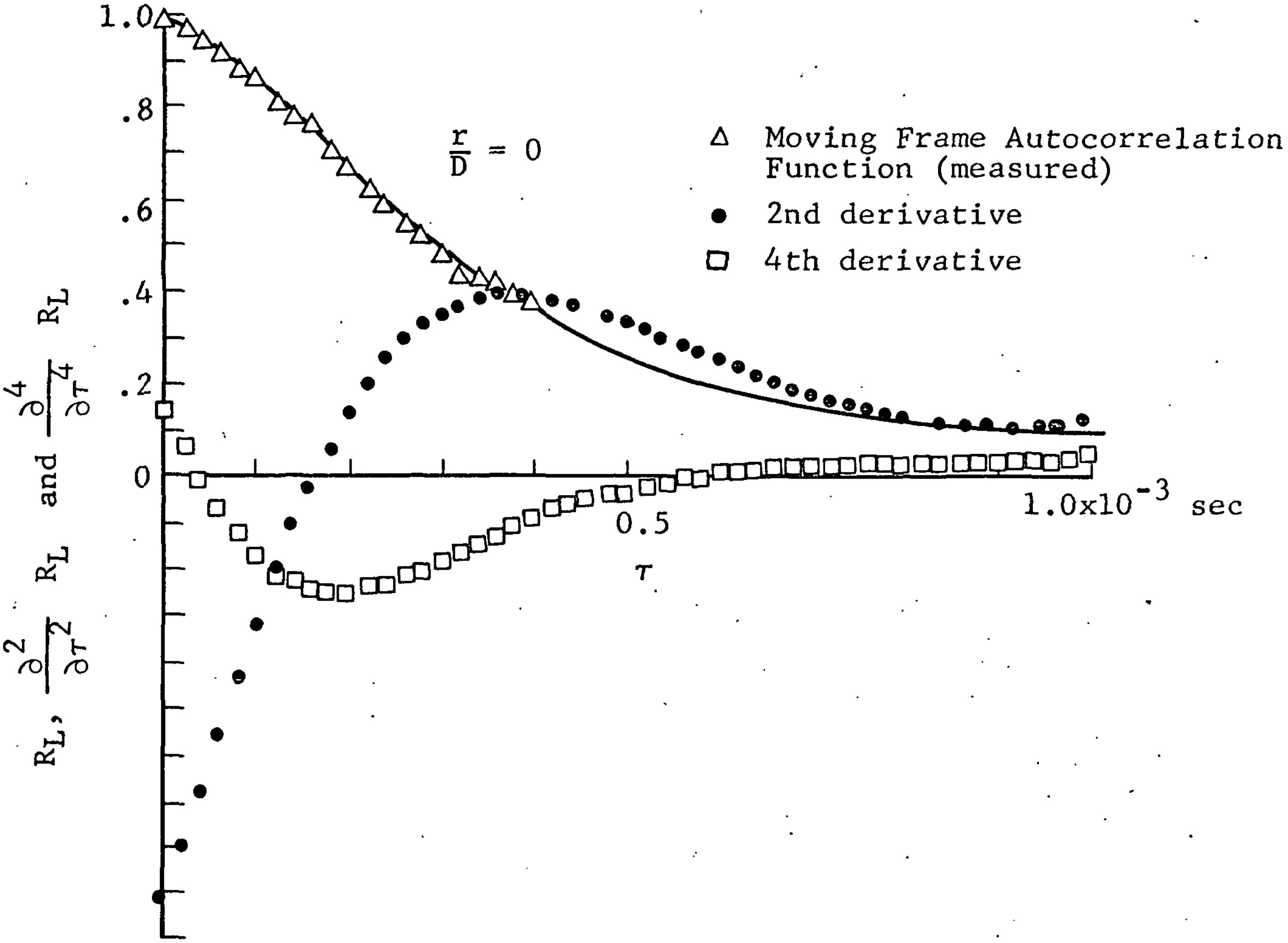

Figure 29a Moving Frame Autocorrelation And Its Derivatives $\frac{y_1}{D} = 6.0$ M = 0.71 Jet

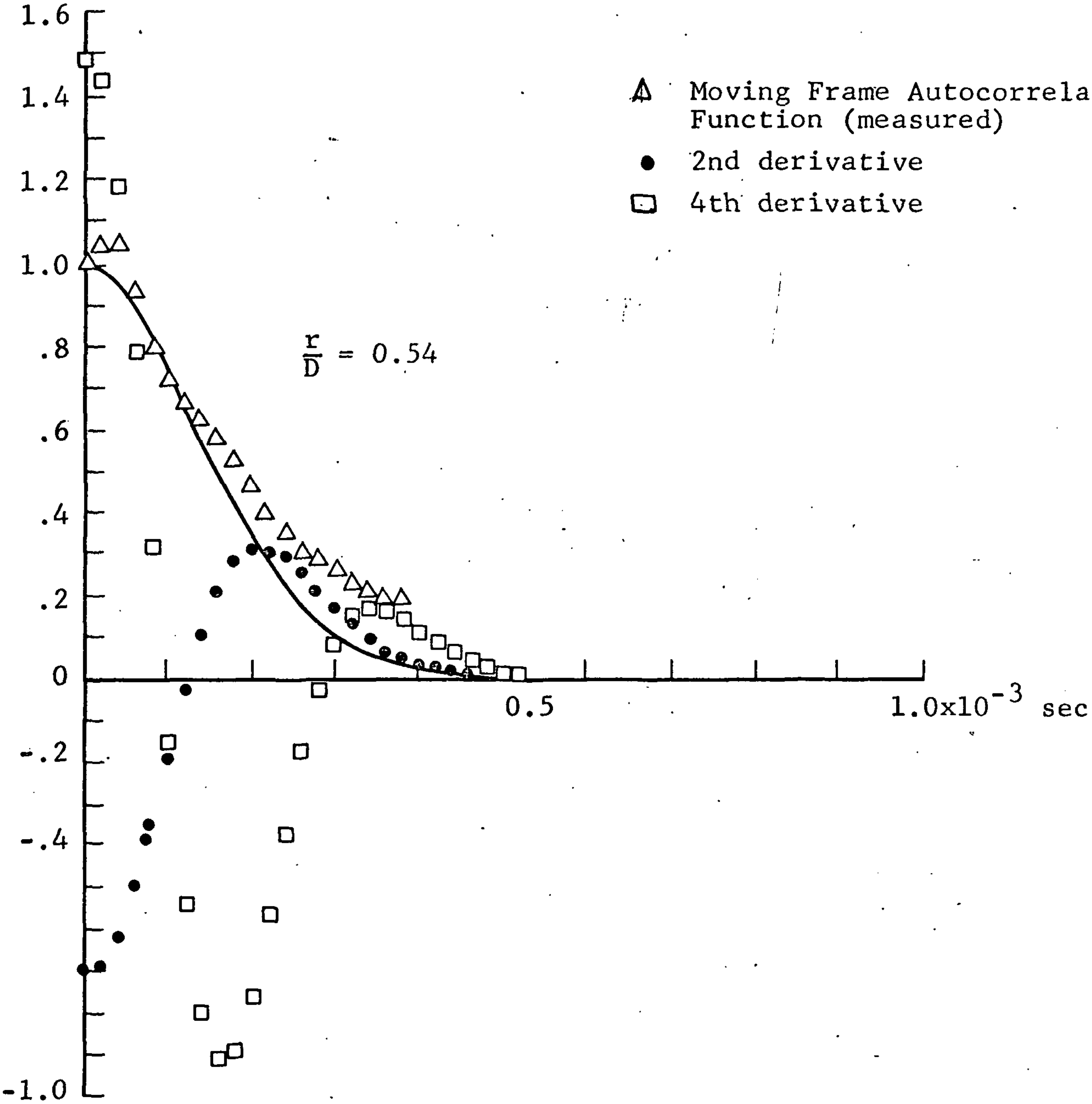

Figure 29b Moving Frame Autocorrelation And Its Derivatives $\frac{y_1}{D}$ = 6.0 M = 0.71 Jet

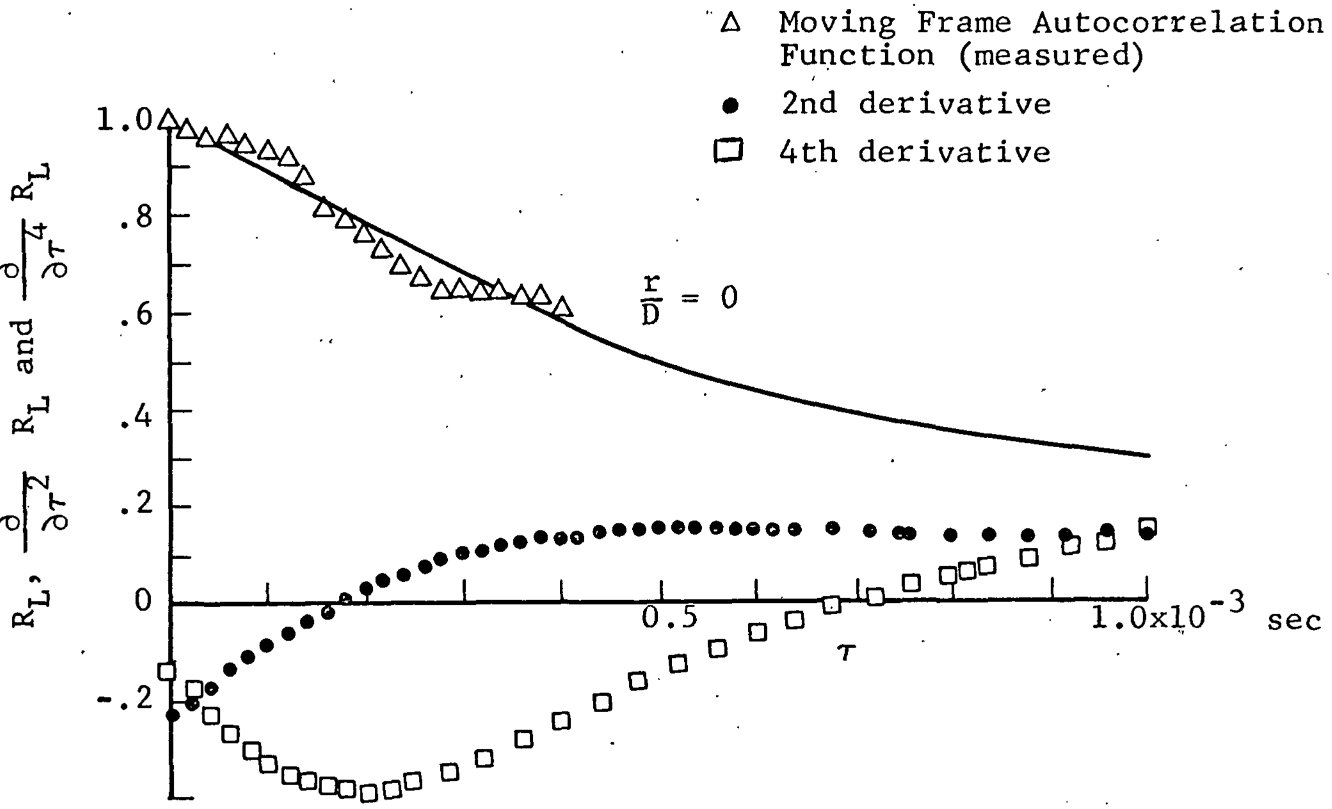

Figure 30a Moving Frame Autocorrelation And Its Derivatives $\frac{y_1}{D}$ = 10.0 M = 0.71 Jet

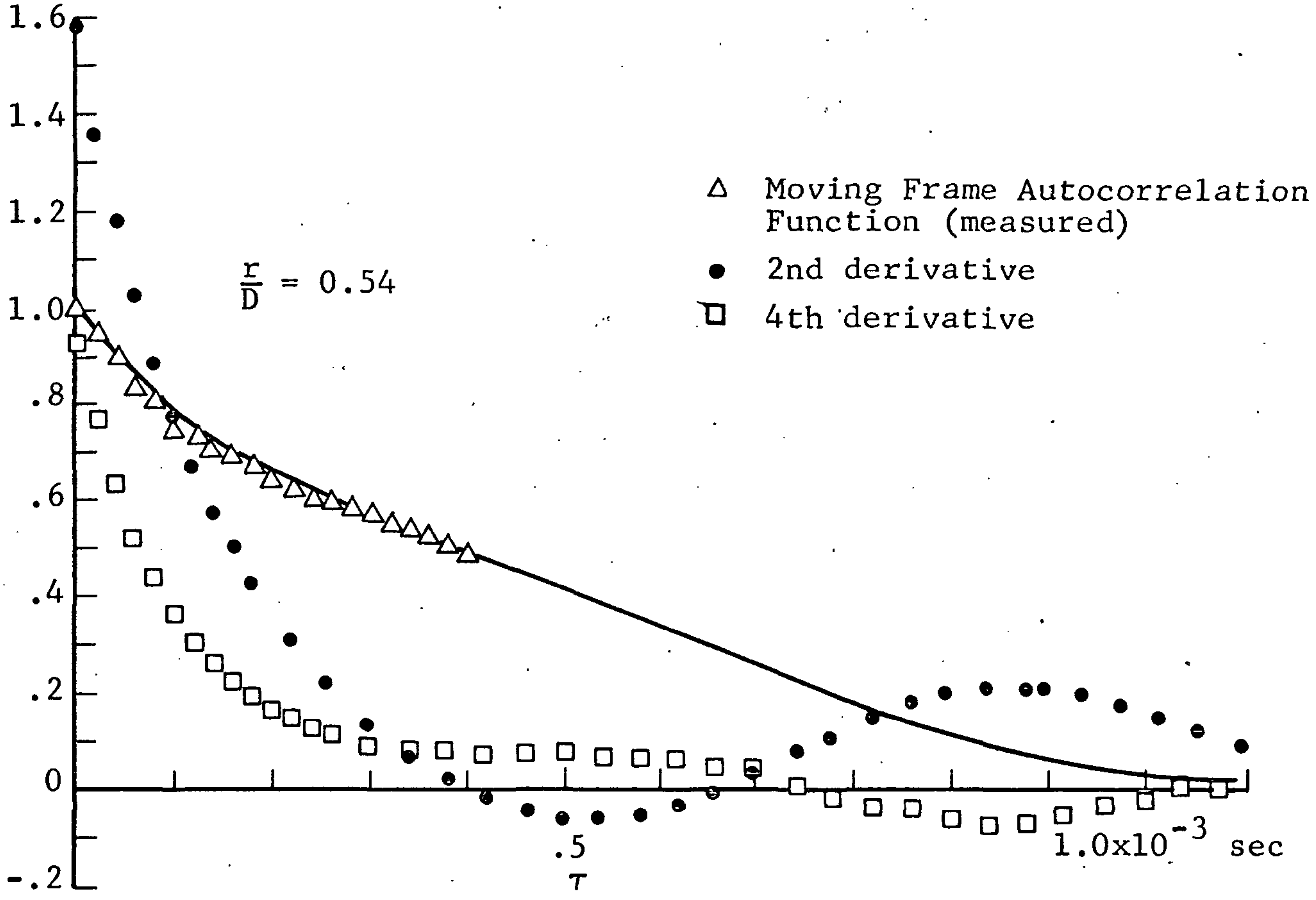

Figure 30b Moving Frame Autocorrelation And Its Derivatives $\frac{y_1}{D} = 10.0$ M = 0.71 Jet

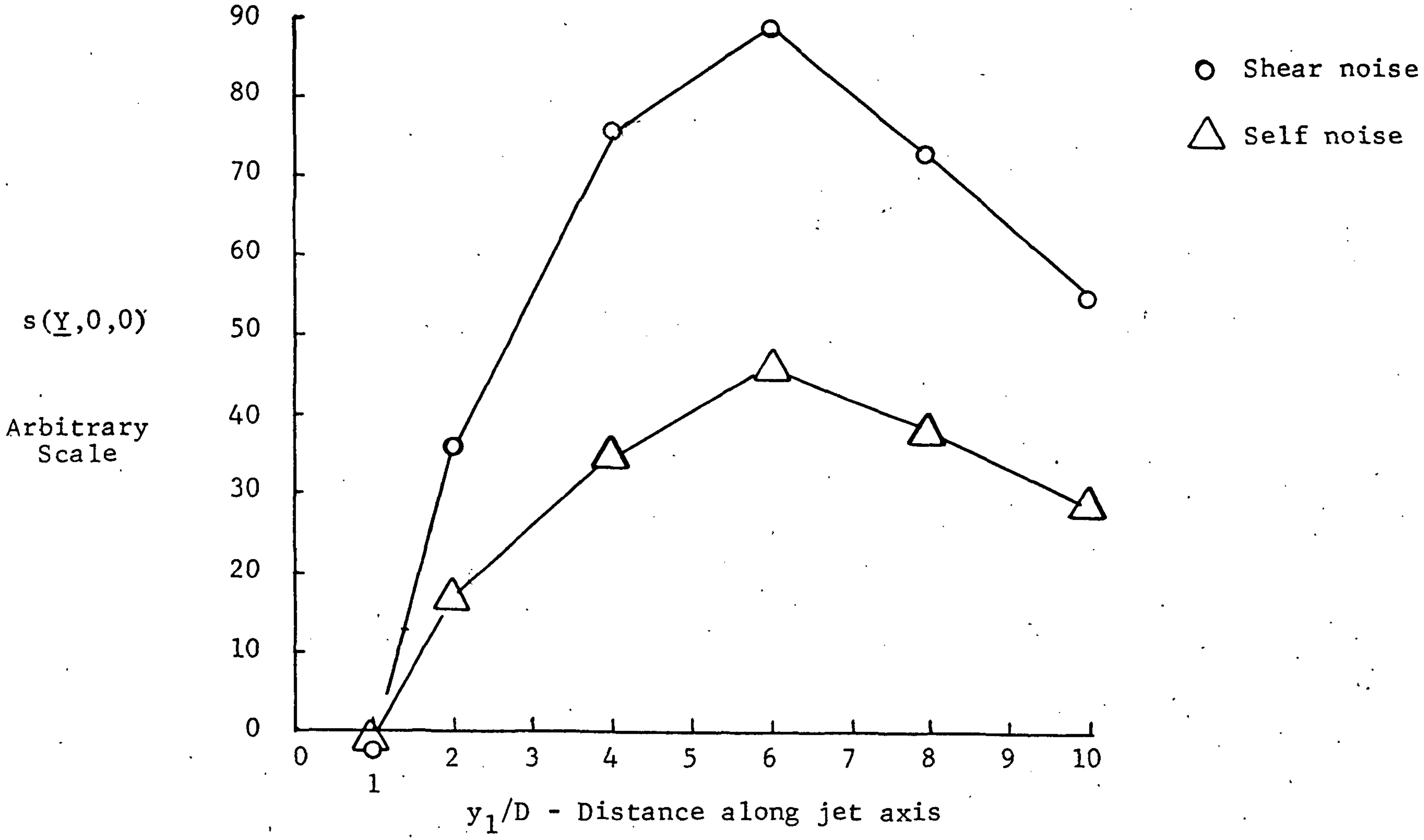

Figure 31 Distribution of Sound Source Intensities (per unit axial distance) - Jet Velocity 315 m/sec

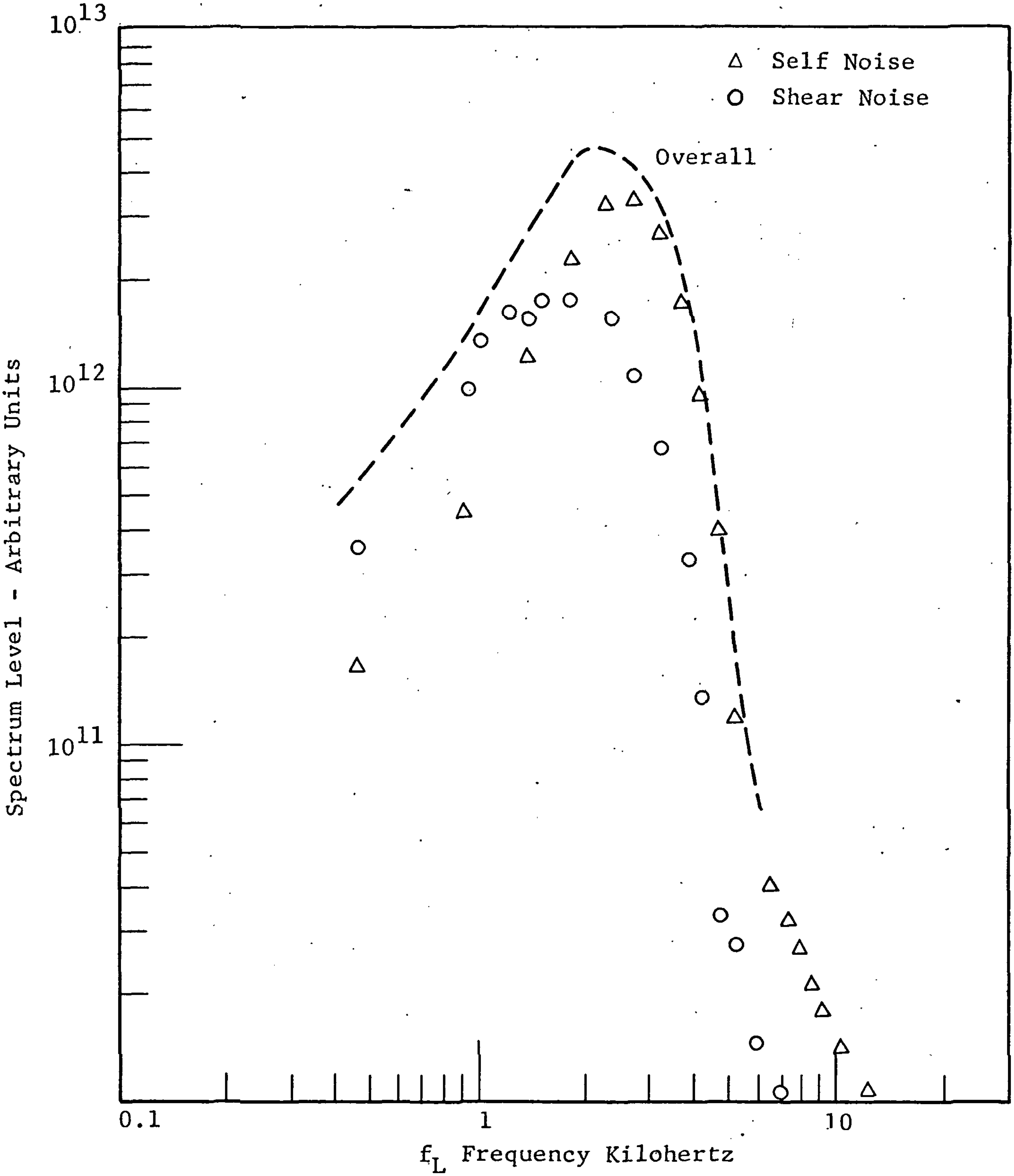

Figure 32 Jet Noise Spectrum Contributed By A Unit Volume Of Turbulence At $y_1/D=6.0$, $r/D= 0.54$

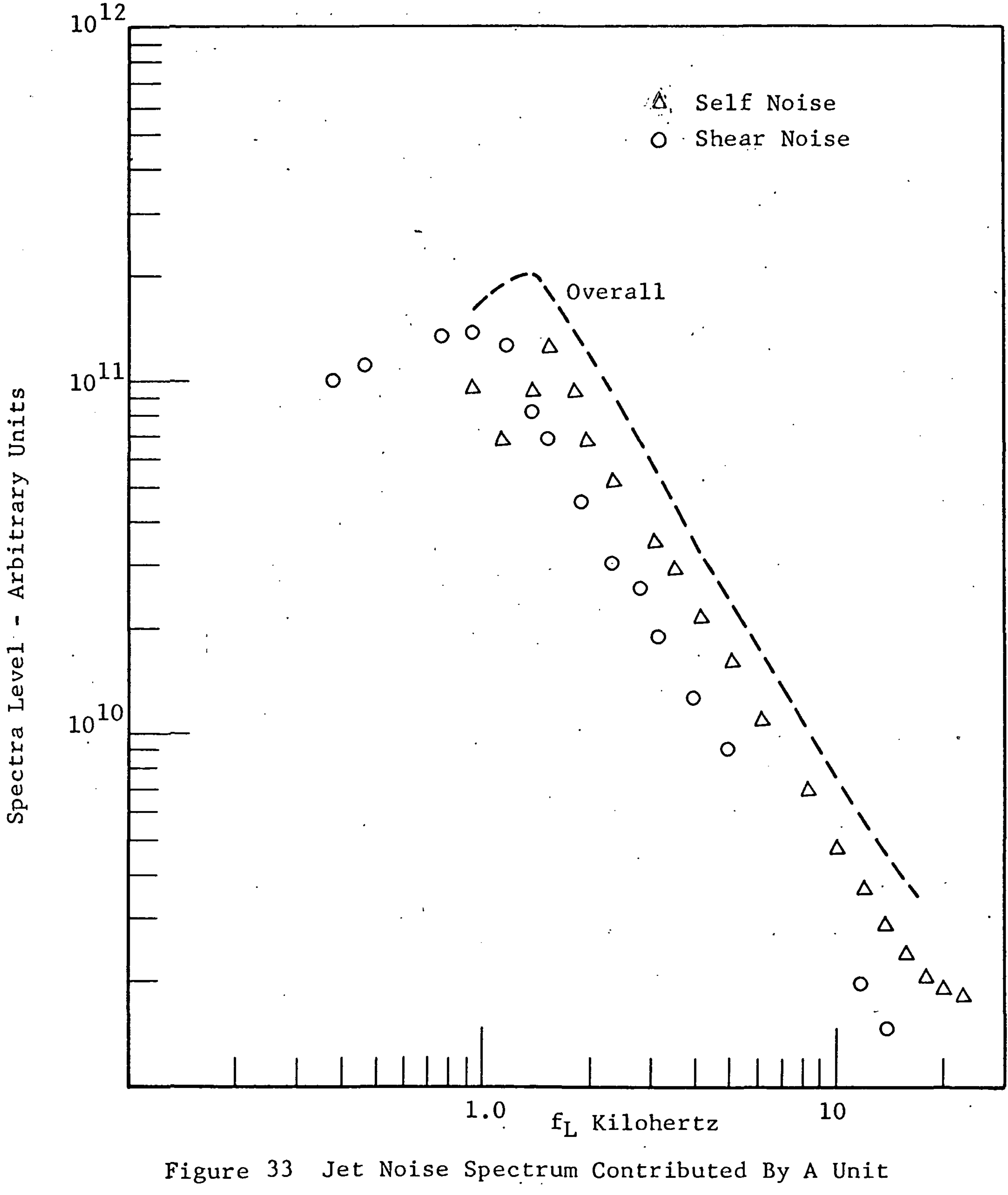

Figure 33 Jet Noise Spectrum Contributed By A Unit Volume of Turbulence At $y_1/D=10.0$, $r/D=0.54$

# REFERENCES

1. Fisher, M.J. and Damkevala, R.J., Fundamental Considerations of the Crossed-Beam Correlation Technique, NASA Contractor Report CR-61252, January 1969.

2. Davis, P.O.A.L., Fisher, M.J. and Barratt, M.J., "The Characteristics of Turbulence in the Mixing Region of a Round Jet," J. Fluid Mech., 15, 337 (1963).

3. Wilson, L.N., Application of Crossed Beam Technology to Direct Measurements of Sound Sources in Turbulent Jets, Final Technical Report J6112 Part I, IIT Research Institute, February 1970.

4. Ribner, H.S., "The Generation of Sound by Turbulent Jets," Advances in Appl. Mech., Vol. VIII, New York, (1964).

5. Wilson, L.N., Analysis of Absorption Cell Data, Interim Report J6186 Part I, IIT Research Institute, March 1970.

6. Chu W.T., "Turbulence Measurements Relevant to Jet Noise" UTIA Report No. 119, Univ. of Toronto, Nov. 1966.

7. Ribner H.S., "On Spectra and Directivity of Jet Noise", J. Acoust. Soc. Amer., 35, 614-616 (1963).

8. Williams J.E. "The Noise from Turbulence Convected at High Speeds" Phil. Trans. Roy Soc. London, Series A 225, 469-503, (1963).

9. Dyer, I. "Distribution of Sound Sources in a Jet Stream", J. Acoust. Soc. Amer. 31, 1016-1021, (1959).

10. Lee, R. "Far Field Measurements of Sound Radiated by Subsonic Air Jets," David Taylor Model Basin, Washington, D.C., DTMB Rep. 868, (1953).

# APPENDIX

# CALIBRATION CELL FOR CROSSED BEAM INSTRUMENT

## 1. BACKGROUND

The cross-correlation technique is useful for the estimation of fluctuating components, mean or static properties are not measured directly by the crossed beam instrument. However, the static properties of the gas do influence the fluctuating absorption coefficient because the absorption derivatives with respect to pressure $(\frac{\partial K}{\partial P})$ and temperature $(\frac{\partial K}{\partial T})$ are functions of the mean gas pressure (P), temperature (T) and concentration of the absorbing species (f) in the gas mixture (Ref. A1) Specifically,

$$\delta K = \left.\frac{\partial K}{\partial P}\right)_{\overline{P},\ \overline{T},\ \overline{f}} \delta P + \left.\frac{\partial K}{\partial T}\right)_{\overline{P},\ \overline{T},\ \overline{f}} \delta T \qquad \text{(A1)}$$

Adiabatic condition gives

$$\frac{\delta T}{T} = \frac{\gamma - 1}{\gamma} \frac{\delta P}{P} \qquad \text{(A2)}$$

where $\gamma$ is the gas constant. Thus we may rewrite, Eq. (1)

$$\delta K = \left[ \left.\frac{\partial K}{\partial P}\right) + \left.\frac{\partial K}{\partial T}\right) \frac{\gamma - 1}{\gamma} \frac{T}{P} \right] \delta P \qquad \text{(A3)}$$

where the partial derivatives are evaluated at the mean levels $\overline{P}$, $\overline{T}$ and $\overline{f}$.

Equation (A3) shows that if known pressure fluctuations can be introduced in a gas, absorption coefficient fluctuations can be calculated if the derivatives $\frac{\partial K}{\partial P}$ and $\frac{\partial K}{\partial T}$ are known at the mean thermodynamic condition of the gas.

The output of the crossed beam correlator which we shall call the cross-correlation function G(x,y,z), is proportional to the mean squared absorption fluctuations within a small correlation volume around the intersection point of the two beams of radiation. If we use superscripts (1) and (2) to identify the two beams,

$$G(x,y,z,\tau) = \overline{i^{(1)}\,(t)\; i^{(2)}\,(t+\tau)}\quad (\text{volts})^2 \tag{A4}$$

where $i^{(1)}(t)$, $i^{(2)}(t+\tau)$ are the a.c. components of the signals at each of the detectors at time t and $t+\tau$ respectively. $i(t)$ is in turn related to the intensity of radiation at the photodetector $\delta I$ after modulation by the absorbing species in the gas. $\delta I$ is related to $\delta K$ by

$$\delta K = -\frac{\delta I}{\ell I} \tag{A5}$$

where $\ell$ is the length of correlation volume through which the beam traverses and I is mean radiation intensity on the photodetector. Hence we can write;

$$G(x,y,z,\tau) = \alpha^2\, \ell^{(1)}\, \ell^{(2)}\, I^{(1)}\, I^{(2)} \left[\overline{\delta K^{(1)}\; \delta K^{(2)}}\right]$$

and

$$G(x,y,z,0) = \alpha^2\, \ell^{(1)}\, \ell^{(2)}\, I^{(1)}\, I^{(2)}\; \overline{\delta K^2} \tag{A6}$$

$\delta K^{(1)} = \delta K^{(2)}$ at the intersection point. $\alpha$ is a calibration factor for the photodetector and its electronics in volts per watt of radiation intensity.

A second calibration factor is now introduced because of the relationship between $\delta K$ and $\delta P$ (or $\delta\rho$) given by Eq.(A3), the constant of proportionality being the terms in the square bracket:

$$\beta = \left.\frac{\partial K}{\partial P}\right)_{\overline{P},\,\overline{T},\,\overline{f}} + \left.\frac{\partial K}{\partial T}\right)_{\overline{T},\,\overline{P},\,\overline{f}} \frac{\gamma-1}{\gamma}\;\frac{T}{P} \tag{A7}$$

Unfortunately $\beta$ is not a well defined constant, but an unknown function of P, T, f and the radiation wavelength and bandpass being employed. Analytical prediction of $\beta$ is extremely complex and impractical. Band models are used to simplify the task somewhat, but this requires assumptions about the content of the data in the form of position and intensity distributions of the included spectral lines.

The most elusive unknowns in all the equations presented so far are the dimensions of the correlation volume, $\ell^{(1)}$, $\ell^{(2)}$, along the beams. This is the volume over which turbulence 'eddy' is coherent and hence contributes significantly to the correlation function. Since density and pressure are scalar quantities, the fluctuations have no direction like velocity fluctuations and hence the concept of the eddy itself is in question. It is these fundamental difficulties along with the complicated nature of $\beta$ in relating the measured quantities to actual turbulent processes that prompts the construction of a calibration cell.

## 2. CELL REQUIREMENTS

The basic requirement of the cell is to produce pressure (or density) fluctuations of known magnitude. The absorption fluctuations resulting from these pressure fluctuations can be measured by the crossed beam instrument and compared with the relationships given in Eqs. (A3), (A6) and (A7) to yield the unknown constants $\alpha$, $\beta$, and $\ell^{(1)}$, $\ell^{(2)}$. It should be noted that the last three 'constants' are functions of the mean thermodynamic state of the gas and hence a relationship should be established between possible thermodynamic states that will be encountered and these constants.

A judicious choice of radiation wavelength and bandpass can be made beforehand to reduce the amount of experimentation. We shall restrict ourselves here to the $4.3\mu$ fundamental absorption band of $CO_2$. By choosing a broad bandpass of $0.08\mu$ the influence of the rotational structure is suppressed while the total energy available is maximized. At the same time, by not using the entire bandwidth of this absorption band, we may be able to minimize or maximize the effects of various thermodynamic states as desired.

Let us consider the use of the cell for calibrating the Crossed Beam Instrument for air jet measurements.

Table A1

| | Min. | Max. | |
|---|---|---|---|
| Gas Pressure | atmos. | 3 atmos. | |
| Gas Temperature | atmos. | 800°F | (427°C) |
| $CO_2$ Concentration | .03 | .06 | percent by volume |
| Pressure Fluctuation Levels | 80 | 160 | dB re .00002 N/m$^2$ |

The possible range of gas conditions is given in Table A1. The pressure fluctuation levels are chosen to provide practical levels measurable with good precision by means of available condenser microphones. One of the shortcomings of previous calibration cell experiments (Ref.A2) was that pressure fluctuations inside the cell were measured by means of a Kistler piezoelectric pressure gauge which introduced excessive noise levels into the measured signals. Secondly, the cell was designed for single optical beam passage only and hence the correlation volume could not be measured. Thirdly, the acoustical characteristics of the measurement chamber were not suited for frequencies above 50 Hz. Fourthly, the cell had its own optical system which could not be used in conjunction with the crossed beam instrument. The present design intends to overcome all these shortcomings.

## 3. EXCITATION PRINCIPLE

The pressure fluctuations will be generated in the calibration cell by means of a loudspeaker. For simplicity and ease of analysis, the discrete frequency acoustic waves should be plane and stationary. This can be achieved in a long tube with a reflecting end, with the speaker coupled at the opposite end by means of a flexible hose. The basic arrangement is shown in Fig.A1. A standing wave pattern is generated inside the tube, fixed at the plane end of the tube.

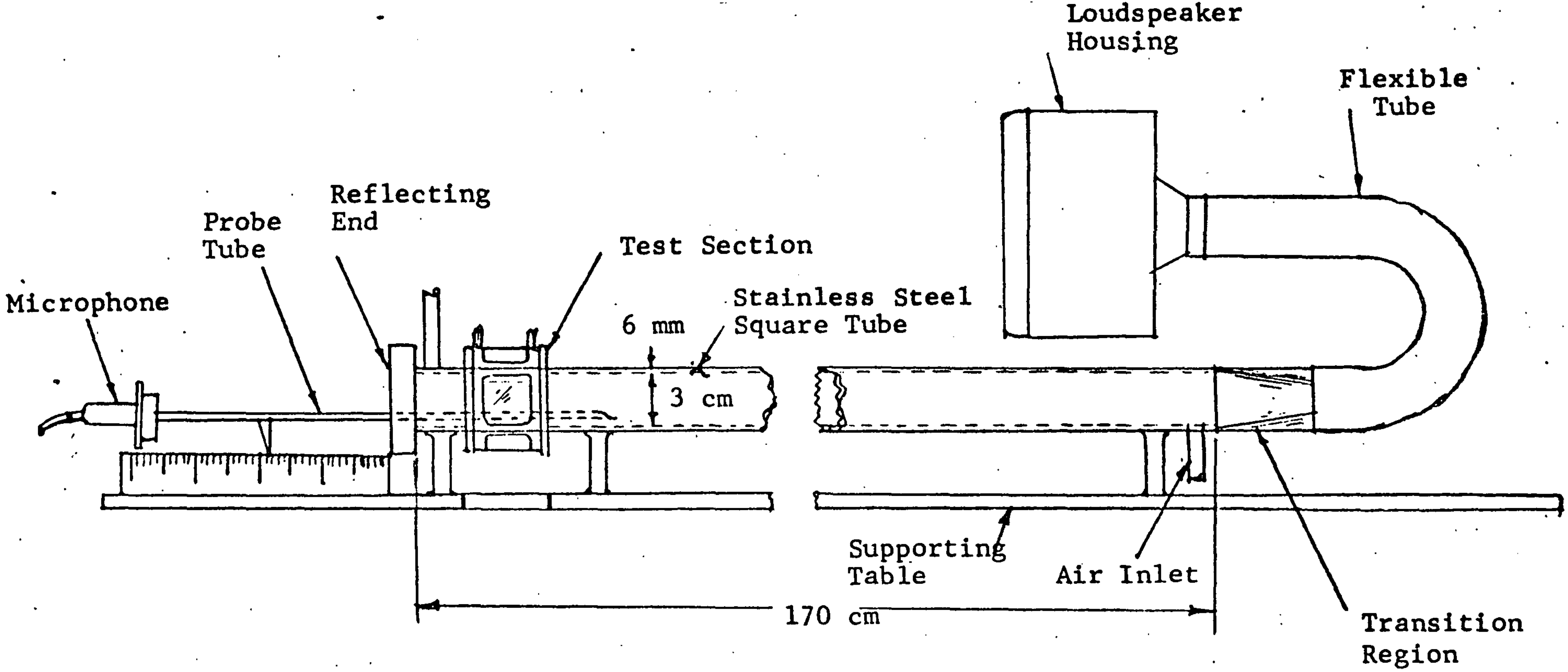

Figure A1 SKETCH SHOWING ARRANGEMENT FOR CALIBRATION CELL

It can be shown that, neglecting losses at the tube wall, the rms amplitude of the pressure $\delta P_1$ is given by (Ref. A1).

$$\delta P_1 = [(A_1+B_1)^2 \cos^2 (k_1 x + \frac{\theta}{2}) + (A_1-B_1)^2 \sin^2 (k_1 x + \frac{\theta}{2})]^{1/2} \tag{A8}$$

where $A_1$ = amplitude of the incident wave

$B_1$ = amplitude of the reflected wave

$\theta$ = phase angle by which the reflected pressure leads or lags the incident pressure wave.

$k_1 = \frac{2\pi f}{c}$ = wave number

c = speed of sound in the medium.

x = distance from reflecting surface

In practice, it is not possible to measure $A_1$, $B_1$ and $\theta$ individually, but if $\delta P_1$ can be measured at three locations near the reflecting surface, the values will be known for all conditions. In fact, this method can also be used for the measurement of normal specific acoustic impedence of a specimen fixed on the reflecting end (Ref. A4). For the present application, the pressure amplitude distribution will be measured by means of a probe microphone inserted through a small hole in the reflecting surface, and compared with the pressure distribution measured with the crossed beam instrument.

According to Beranek (Ref. A4), to assure plane waves, the inside diameter of a cylindrical tube should not exceed the value given by

$$d = \frac{20,000}{f_h} \text{ cm} \tag{A9}$$

where $f_h$ is the highest frequency at which measurements are to be made. Because of the requirement for the crossed beam to pass undistorted through the tube, a square tube of inside dimensions 3 cm x 3 cm is recommended. Such a tube would be useful to at least 5 kHz at room temperature. The length of the tube should be not less than half the wavelength of the lowest frequency at which measurements are to be made. A 170 cm length will therefore be adequate down to 100 Hz. The operating frequencies will have to be chosen from this 100 Hz to 5 kHz range, and will probably be selected from the resonant frequencies in the tube.

## 4. DRIVER

Assuming an average efficiency of a loudspeaker to be 20 percent, we can compute the electrical power rating of the speaker for exciting the acoustic field in the tube to the maximum pressure levels of 160 dB. Actually the efficiency is expected to be greater at the resonant frequencies in the cell.

$$160 \text{ dB} = 20 \log_{10} \frac{\delta P_1}{2\text{x}10^{-5}}$$

$$\delta P_1 = 2\text{x}10^{-5} \text{ x } 10^8 = 2\text{x}10^3 \text{ N/m}^2 \text{ rms}$$

$$\text{Intensity} = I = \frac{\delta P_1^2}{\rho_o c}$$

$$= .964 \text{ x } 10^4 \text{ watt/m}^2$$

Hence acoustic power required = I(cross-sectional area of tube)

$$= .964\text{x}10^4 \text{ x } 9\text{x}10^{-4} \quad = 8.7 \text{ watts}$$

Assuming efficiency = .20,

Electrical power = 43.5 watts

Hence a speaker rated at 50 watts continuous would be adequate. A possible candidate would be University Ling-Altec Model ID-50 acoustic horn driver.

## 5. PROBE MICROPHONE

The probe tube should be made of small diameter for two reasons. First, the tube area should be small compared to the cell cross section to minimize its influence on the standing wave pattern. Secondly, a small internal diameter will damp out strong resonances likely to occur inside the probe tube. A stainless steel tubing with internal and external diameters of 0.241 and 0.316 cm, respectively, and a length of 50 cm would be suitable. One end of the tube should be connected to a small cavity about 2 cc in volume, in front of a 1/2 inch condenser microphone enclosed in an aluminum housing. The tube should be connected by means of a short sleeve of flexible tubing to prevent transmission of vibrational components from the wall of the probe to the microphone. This flexible tubing as well as the microphone diaphragm should be able to withstand the highest gas temperature that will be used in the cell. Figure 2 shows one possible arrangement for coupling the probe tube to a condenser microphone. The probe tube can be calibrated by alternately placing the probe and a 1/8 inch microphone in an anechoic sound field at various frequencies.

## 6. WINDOWS

Circular (or square) windows of 2.5 cm principal dimension should be provided at a distance of 10 cm from the reflecting end. Irtran or sapphire ($A\ell_2O_3$) windows about 2 mm thick, can be used. The windows should be optically flat and mounted parallel to avoid disturbing the crossed beam instrument alignments. The window mounting design will need special attention to allow for the thermal expansion due to heating the cell. It might become advantageous to make the window assembly with a double wall with water circulation for cooling as it would also lower the thermal emission of the windows into the crossed beam system. This item may need further research before the design is finalized.

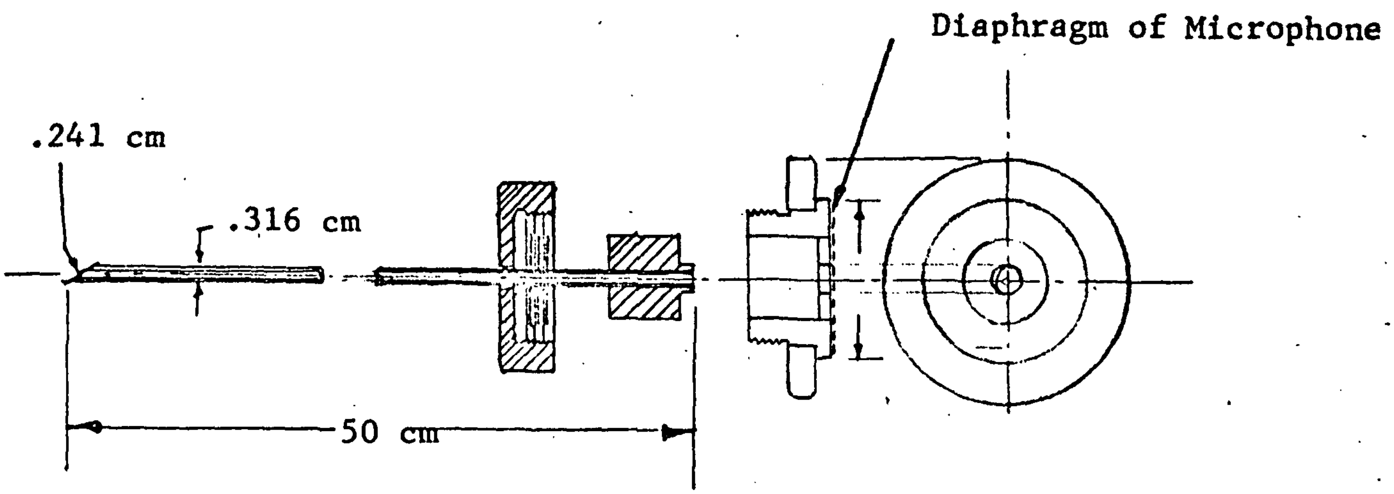

Figure A2 PROBE TUBE AND MICROPHONE COUPLER

## 7. CELL TEMPERATURE CONTROL

It is desirable to maintain a uniform temperature throughout the gas enclosed in the cell. Even small changes in temperature would produce changes in the standing wave pattern which would be detected by the sensitive crossed beam instrument. A change in temperature by 1°R at 500°R results in a change in sound wavelength of 6 mm. Hence the first nodal point after reflection would move a distance of 3 mm. Temperature control might prove to be the most critical feature of the calibration cell at short wavelengths and lower temperatures. A constant temperature liquid bath can be provided around the cell to regulate the cell temperature in the low temperature range. See for example, Beranek (Ref. A4 & A5).

To achieve the higher temperatures necessary for calibration prior to heated jet studies, thermostatically controlled electrical heating tapes can be wrapped around the metal tube. The spacing and width of the tape can be controlled to achieve uniformity of temperature inside the tube. Also, sections of the tape can be supplied with varying currents to achieve uniformity of temperature. Unless the temperature is maintained uniform throughout the tube, thermal equilibrium will not be achieved, and accurate measurements will be impossible. The degree of uniformity necessary will have to be determined experimentally; the maximum appears to be about 1°F per cm.

Thermocouples should be embedded in the sides of the tube at several locations to monitor the temperature. In addition, a temperature probe can be used to check the gas temperatures on the axis of the tube.

## 8. MECHANICAL

Provision should be made to allow precise positioning of the probe microphone with respect to the calibration cell. The long square tube should be positioned so that the crossed infrared beams pass through the windows. For this reason a sturdy stand will be necessary, with provision for fine adjustment of height.

The speaker should be enclosed in a housing by itself and connected to the resonance tube by means of a flexible tube and a conical coupler. A transition region will be required between the square tube and the round loudspeaker tube. The tube itself should be made of 6 mm thick stainless steel with inner dimensions of 3 x 3 x 170 cm. Suitable ports for filling and venting the test chamber should be provided.

The window region may be fabricated separately with a double wall for circulating water for cooling. The entire cell may require some form of constant temperature bath if temperature gradients prove to be a problem.

## 9. ESTIMATION OF SCALES $\ell^{(1)}$, $\ell^{(2)}$

In scalar fields the scales are related to the spectrum of fluctuations. Hence if the sound field in the cell has the same spectrum as the turbulence to be measured by the crossed beam, a measure of the length scales will be obtained. Difficulties are immediately apparent, because the tube acts as a resonator and it would be impossible to produce a sound spectrum of the desired shape in it. Hence we will have to be content with measuring the apparent scales at discrete frequencies and infer the actual turbulent scales from a spectrum analysis of the turbulence. Fortunately the correlation volume is weighted by the size of the radiation beams at the intersection point and hence this frequency effect may not be pronounced.

## 10. INFRARED SPECTROSCOPY

It is our purpose to evaluate the function $\beta$ given by Eq.A7). As mentioned previously, $\beta$ is a complicated function of mean properties of the gas $\overline{P}$, $\overline{T}$ and $\overline{f}$ through the partial derivatives $\frac{\partial K}{\partial P}$ and $\frac{\partial K}{\partial T}$. Some results of earlier experiments are available to us for guidance. These are summarized below. In all cases, a spectroscopic bandwidth of .08$\mu$ is assumed.

At 4.20$\mu$, $\delta K$ is a function of $\delta P$ only for pressures from 422 to 1053 mm Hg ($5.63 \times 10^4$ to $14.05 \times 10^4$ N/m$^2$) and temperatures from 243 to 393°K at a given $CO_2$ concentration f. The f dependence is given by a power low relationship with an exponent 0.76. At 4.35$\mu$, $\delta K$ is independent of P but strongly dependent on both T and f. Since f is known from the measurement at 4.20$\mu$, the measurement at 4.35$\mu$ will yield temperature. The temperature dependence can also be represented by a power law with an exponent $\simeq 1.5$.

The value of $\frac{\partial K}{\partial T}$ remains constant for all T at 4.30$\mu$ but drops slightly with increasing f. For normal atmospheric $CO_2$ concentration f = .03%, $\frac{\partial K}{\partial T} = -5 \times 10^{-7}$ for $500 < P < 1000$ mm Hg., while at f = .121%, $\frac{\partial K}{\partial T}$ $-11 \times 10^{-7}$. The unit of K is mm$^{-1}$.

The pressure derivative $\frac{\partial K}{\partial P}$ is positive for all combinations of the parameters. At 4.30$\mu$, 297°K and .03% concentration, $\frac{\partial K}{\partial P} = 6.0 \times 10^{-7}$.

## 11. CONCLUDING REMARKS

A conceptual design for a calibration cell for crossed beam infrared measurements has been presented. It is hoped that the cell will answer many of the questions relating to the application of the crossed beam correlation technique for jet noise prediction.

# 12. REFERENCES

A 1. Lysobey, David J., "Infrared Correlation Spectroscopy with Application to $CO_2$ Under Atmospheric Conditions," Ph.D. Thesis, University of Oklahoma, 1972.

A 2. Cann. M.W.P., Absorption Calibration Cell - Instruction Manual, Report J6113-V06, IIT Research Institute, Sept. 1969.

A 3. Kinsler and Frey, Fundamentals of Acoustics, 2nd Edition, John Wiley & Sons, New York, 1962.

A 4. Beranek, L. L., Acoustic Measurements, John Wiley & Sons, New York, 1949.

A 5. Beranek, L. L., "Some Notes on the Measurement of Acoustic Impedance," Jour. Acoust. Soc. America, 19, pp. 420-427 (1947).